



1 Satellite Passive Microwave Sea-Ice Concentration Data Set Inter- 2 comparison using Landsat data

3
4 Stefan Kern¹, Thomas Lavergne², Leif Toudal Pedersen³, and Rasmus Tage Tonboe^{4a}, Louisa Bell^{1b},
5 Maybritt Meyer^{1c}, and Luise Zeigermann^{1d}

6
7 ¹Integrated Climate Data Center (ICDC), Center for Earth System Research and Sustainability (CEN), University of Hamburg,
8 Hamburg, Germany

9 ²Research and Development Department, Norwegian Meteorological Institute, Oslo, Norway

10 ³Danish Technical University, Lyngby, Denmark

11 ⁴Danish Meteorological Institute, Copenhagen, Denmark

12 ^anow at Danish Technical University, Lyngby, Denmark

13 ^bnow at Climate Service Center Germany (GERICS), Helmholtz-Zentrum Hereon, Hamburg, Germany

14 ^cnow at Federal Maritime and Hydrographic Agency, Hamburg, Germany

15 ^dnow at Faculty of Science for Physics and Physical Oceanography, Memorial University of Newfoundland, St. Johns, Canada

16 *Correspondence to:* Stefan Kern (stefan.kern@uni-hamburg.de)

17 **Abstract.** We report on results of an inter-comparison of 10 global sea-ice concentration (SIC) data products at 12.5 to 50.0
18 km grid resolution from satellite passive microwave (PMW) observations. For this we use SIC estimated from > 300 images
19 acquired in the visible / near-infrared frequency range by joint the National Aeronautics and Space Administration
20 (NASA)/United States Geological Survey (USGS) Landsat sensor during years 2003-2011 and 2013-2015. Conditions covered
21 are late winter / early spring in the Northern Hemisphere and from late winter through fall freeze-up in the Southern
22 Hemisphere. Among the products investigated are the four products of the European Organisation for the Exploitation of
23 Meteorological Satellites (EUMETSAT) Ocean and Sea Ice Satellite Application Facility (OSI SAF) and European Space
24 Agency (ESA) Climate Change Initiative (CCI) algorithms: SICCI-2 and OSI-450. We stress the importance to consider inter-
25 comparison results across the entire SIC range instead of focusing on overall mean differences, and to take in account known
26 biases in PMW SIC products, e.g. for thin ice. We find superior linear agreement between PMW SIC and Landsat SIC for the
27 25 km and the 50 km SICCI-2 products in both hemispheres. We discuss quantitatively various uncertainty sources of the
28 evaluation carried out. First, depending on the number of mixed ocean-ice Landsat pixels classified erroneously as ice only,
29 our Landsat SIC is found to be biased high. This applies to some of our Southern Hemisphere data, promotes an overly large
30 fraction of Landsat SIC under-estimation by PMW SIC products, and renders PMW SIC products overestimating Landsat SIC
31 particularly problematic. Secondly, our main results are based on SIC data truncated to the range 0 % to 100 %. We demonstrate
32 using non-truncated SIC values, where possible, can considerably improve linear agreement between PMW and Landsat SIC.
33 Thirdly, we investigate the impact of filters often used to clean up the final products from spurious SIC over open water due
34 to weather effects and along coastlines due to land spillover. Benefiting from the possibility to switch on or off certain filters
35 in the SICCI-2 and OSI-450 products we quantify the impact land spillover filtering can have on evaluation results as shown
36 in this paper.

37 1 Introduction

38 We carry on the evaluation of sea-ice concentration (SIC) products derived from satellite passive microwave (PMW)
39 observations. In Kern et al. (2019), we presented an evaluation of ten PMW SIC products at 0 % and 100 % SIC, and with
40 respect to sea-ice observations along ship tracks. Another study focused on Arctic summer conditions, investigating the bias
41 between these PMW SIC products and independent SIC and net ice surface fraction estimates based on MODerate resolution
42 Imaging Spectroradiometer (MODIS) observations (Kern et al., 2020). With this study, we shift our focus more towards
43 intermediate SIC and utilize are much larger and, partly, more accurate reference dataset than in the two earlier studies. The



44 evaluation at 0 % SIC in Kern et al. (2019) used a few fixed open water locations only. The evaluation at 100 % SIC used
45 near-100 % SIC estimates based on the analysis of freezing-season synthetic aperture radar (SAR) image pairs of convergent
46 high-concentration ice situations. With that we evaluated the PMW SIC products for one specific set of ice conditions only
47 (winter and near 100 %). Kern et al. (2019) also presented results of an evaluation of PMW SIC against a multi-annual set of
48 standardized manual visual ship-based observations of the ice conditions. These observations are, however, of limited accuracy
49 and of limited representativity because the average accuracy is between 5 % and 10 % and observations mostly represent sea-
50 ice conditions where it is possible to navigate. In addition, to reduce noise, PMW and ship-based SIC were averaged over all
51 observations along a ship-track within one day, representing sea-ice conditions across spatial scales, that – in the worst case –
52 vary by an order of magnitude. The averaging resulted in a reduction of the number of valid data pairs from about 15000 to
53 less than 800, i.e. about 400 per hemisphere.

54 Another aspect is that the accuracy of the hemispheric but also the regional sea-ice area (SIA) computed from PMW
55 SIC estimates strongly depends on their accuracy. PMW SIC values biased high yield an overestimation of the SIA whereas
56 PMW SIC biased low results in an underestimation of the SIA. This seems not to be critical as long as the trend is correct (e.g.
57 Ivanova et al., 2014) but limits the use of such SIA estimates for quantitative inter-comparisons of climate-model results
58 against observations (e.g. Burgard et al., 2020). It is for sure important PMW SIC is 100 % where the actual SIC is 100 % to
59 avoid artificially elevated ocean-atmosphere heat flux when used as a surface forcing. It is equally important PMW SIC is an
60 accurate estimate of the open water fraction, hence providing 95 % where the actual SIC is 95 % due to leads and openings in
61 the sea-ice cover. In addition, it is desirable to check the performance of PMW SIC products across the entire SIC range in
62 order to have a reliable estimate of the actual ice cover in, for example, the marginal ice zone (MIZ). Here gradients in heat
63 fluxes are particularly pronounced and small changes in the SIC can have a comparably large impact on ocean-atmosphere
64 heat transfer. A correct definition of and accurate SIC distribution within the MIZ are also crucial should SIC values be used
65 to evaluate numerical models capable to simulate wave-sea ice interaction (e.g. Boutin et al., 2020; Nose et al., 2020). The
66 ship-based SIC observations used in Kern et al. (2019) offer only limited potential to carry out this performance check because
67 of i) their accuracy and limitations in spatial representativity, ii) the small number of observations falling into the relevant SIC
68 range of, e.g. 20 % to 80 %, and iii) the larger observational error in this SIC range.

69 Therefore, in this paper we focus on the evaluation of PMW SIC products against a large number of high-resolution
70 binary sea-ice cover maps estimated from satellite observations acquired in the visible frequency range by NASA/USGS
71 Landsat-5, 7 and 8. Overall, we used over 300 such Landsat-based maps, corresponding to more than 10 000 25 km x 25 km
72 resolution PMW SIC grid cells. We chose Landsat over MODIS because of the substantially finer spatial resolution of the
73 visible channels of Landsat: 30 m compared to MODIS: 250 m. Another option would have been to use Sentinel-2
74 MultiSpectral Instrument (MSI) (Drusch et al., 2012). We discarded this option in light of the limited overlap between this
75 satellite mission (Sentinel-2A was launched June 2015) and our PMW SIC data set but it will be very valuable in the future
76 since it will allow extending the dataset to areas much further from land and will likely provide an even more accurate
77 evaluation data set.

78 Utilization of the high-resolution information provided by the Landsat satellites as a means for assessing satellite
79 PMW SIC products dates back to the early 1980ties when Comiso and Zwally (1982) compared Nimbus-7 Scanning
80 Multichannel Microwave Radiometer (SMMR) SIC with Landsat imagery. Since then a number of studies used a small number
81 of such images for inter-comparison and/or evaluation studies of SIC retrievals (e.g. Steffen and Maslanik, 1988; Steffen and
82 Schweiger, 1991; Comiso and Steffen, 2001; Cavalieri et al., 2006; Wiebe et al., 2009; Lu et al., 2018; Zhao et al., 2021).
83 Landsat imagery has also recently been used for quality assessment of SIC estimates from Suomi/NPP VIIRS observations
84 (e.g. Liu et al., 2016). Common to all these studies is they used a comparably small number of Landsat scenes, i.e. less than
85 ten, an order of magnitude smaller than the number of scenes used in this study (see above).



86 Analysis of visible satellite imagery for SIC estimation is quite straightforward. A threshold based method
87 discriminating between open water and ice is applied at the native spatial resolution (pixel size: 30 m x 30 m) of the Landsat
88 channels in the visible frequency range, assuming that a pixel is covered by either ice or water. Co-locating this high-resolution
89 information of the binary ice-water distribution with the coarse-resolution PMW SIC products and counting ice and water
90 pixels within a PMW SIC product's grid cell provides an adequate independent measure of the SIC. We refer to Section 2.2
91 for more details.

92 For evaluating the PMW SIC products across the SIC range, we prefer to use visible data instead of SAR data. The
93 main advantages of SAR data would be i) the larger area covered by a single scene compared to Landsat (about 400 km to 500
94 km in SAR wide-swath mode (WSM) vs. 180 km for Landsat) and ii) their independence to daylight and cloud cover. In fact,
95 many PMW SIC inter-comparison studies have already used SAR images (e.g., Comiso et al., 1991; Dokken et al., 2000;
96 Belchansky and Douglas, 2002; Kwok, 2002; Heinrichs et al., 2006; Andersen et al., 2007; Wiebe et al., 2009; Han and Kim,
97 2018). However, despite the past decade's substantial progress in developing and testing methods to translate SAR images into
98 high-resolution SIC maps (e.g.: Cooke and Scott, 2019; Karvonen, 2014, 2017; Komarov and Buehner, 2017, 2019; Leigh et
99 al., 2014; Lohse et al., 2019; Ochilov and Clausi, 2012; Singha et al., 2018; Wang et al., 2016, 2017; Zakhvatkina et al., 2017,
100 Boulze et al., 2020; Malmgren-Hansen et al., 2020; Wang and Li, 2020), some using machine learning approaches, the accuracy
101 of the obtained SIC maps is not always satisfying. Particularly at intermediate SIC – the main focus of this study – SAR
102 signatures are often ambiguous, resulting in SAR SIC uncertainties too large for our purposes. Furthermore, applications of
103 such methods to derive Southern Ocean SIC from SAR are comparably sparse. Therefore, we do not use SAR-based SIC maps.

104 We note that also Ice charting services (FMI, DMI, MET Norway, CIS, NATICE, AARI) heavily depend on SAR
105 imagery for production of their ice charts. They thus have a large demand to automate processes of classification and are
106 potentially most advanced in testing automated SAR SIC retrieval (e.g. Cheng et al., 2020). However, ice charts provide SIC
107 ranges within polygons highly variable and heterogeneous in size and shape. Several studies used such ice charts for various
108 inter-comparison purposes (e.g. Shokr and Markus, 2006; Shokr and Agnew, 2013, Titchner and Rayner, 2014). Some centers
109 providing operational sea-ice information also use such charts for routine quality checking of PMW SIC products. However,
110 for our purpose evaluating PMW SIC CDRs and similar SIC products, the limitations of such charts in terms of precision and
111 accuracy – particularly in the intermediate SIC range (e.g. Cheng et al., 2020), exclude their usage in this study.

112 After this introduction, this paper provides information about the PMW SIC products, the Landsat data set used and
113 the methods applied to derive SIC from the Landsat images (Sect. 2). We present our results in Sections 3 and 4, discuss some
114 additional aspects in Section 5 and conclude the study in Section 6.

115 **2 Data & Methodologies**

116 **2.1 Sea-ice concentration data sets**

117 The ten different PMW SIC products considered in our study are summarized briefly in Table 1. We refrain from
118 repeating information about the algorithms themselves, tie point selection, application of weather filters, consideration of land
119 spillover effects and so forth. All this information is provided in detail in Lavergne et al. (2019), Kern et al. (2019, Appendix
120 7.1-7.6), and Kern et al., (2020). The same applies to the fact that four of the products (SICCI-12km, SICCI-25km, SICCI-
121 50km, and OSI-450) allow to take into account the full SIC distribution at the two end-member sea-ice concentrations: 0 %
122 and 100 % which naturally result from the SIC retrieval method used in all considered SIC products but the NT2-AMSR
123 product. This distribution contains negative as well as above-100 % SIC values that are typically truncated, i.e. set to the
124 exactly 0 % and 100 %. We refer to Lavergne et al. (2019) and Kern et al. (2019) for more information in this regard.

125 In order to extend the time-series of the Comiso Bootstrap (CBT) algorithm and the NASA-Team 2 (NT2) algorithm
126 using Advanced Microwave Scanning Radiometer aboard Earth Observation Satellite (AMSR-E) data beyond its lifetime



127 (2011-10-03), we use the respective unified product based on data of the Advanced Microwave Scanning Radiometer aboard
 128 GCOM-W1: AMSR2 and of AMSR-E (Meier et al., 2018). With that we use five products based on AMSR-E and AMSR2
 129 data and five products based on Special Sensor Microwave / Imager: SSM/I, and Special Sensor Microwave Imager and
 130 Sounder: SSMIS data, of the period 2002 through 2015. We do not use PMW SIC data of the period October 2011 through
 131 July 2012 because of the gap between AMSR-E and AMSR2. All PMW SIC data have daily temporal resolution. The grid
 132 type and grid resolution of all datasets are provided in Table 1.

133

134 **Table 1.** Overview of the investigated PMW SIC products. Column “ID (Algorithm)” holds the identifier we use henceforth
 135 to refer to the data product, and which algorithm it uses. Note that for those algorithms where an AMSR sensor forms part of
 136 the name, we refer to AMSR-E or AMSR2, depending on which of the two sensors provides the data. Column “Input data”
 137 refers to the input satellite data for the data set, together with the frequencies and respective field-of-view dimensions.
 138

ID (algorithm)	Input data; frequencies (field-of-views)	Grid resolution & type	Reference
OSI-450 (SICCI2)	SSM/I, SSMIS; 19.35 GHz (69 km x 43 km), 37.0 GHz (37 km x 28 km)	25 km x 25 km EASE2.0	Tonboe et al., 2016; Lavergne et al., 2019
SICCI-12km (SICCI2)	AMSR-E/AMSR2; 18.7 GHz (27 km x 16 km/ 22 km x 14 km), 89.0 GHz (6 km x 4 km/ 5 km x 3 km)	12.5 km x 12.5 km EASE2.0	Lavergne et al., 2019
SICCI-25km (SICCI2)	AMSR-E/AMSR2; 18.7 GHz (27 km x 16 km/ 22 km x 14 km), 36.5 GHz (14 km x 8 km/ 12 km x 7 km)	25 km x 25 km EASE2.0	Lavergne et al., 2019
SICCI-50km (SICCI2)	AMSR-E/AMSR2 6.9 GHz (75 km x 43 km/ 62 km x 35 km), 36.5 GHz (14 km x 8 km/ 12 km x 7 km)	50 km x 50 km EASE2.0	Lavergne et al., 2019
CBT-SSMI (Comiso bootstrap)	SSM/I, SSMIS; 19.35 GHz (69 km x 43 km), 37.0 GHz (37 km x 28 km)	25 km x 25 km PolarStereo	Comiso, 1986; Comiso et al., 1997; Comiso and Nishio, 2008
NOAA-CDR (NASA Team & Comiso bootstrap)	SSM/I, SSMIS; 19.35 GHz (69 km x 43 km), 37.0 GHz (37 km x 28 km)	25 km x 25 km PolarStereo	Peng et al., 2013; Meier and Windnagel, 2018
CBT-AMSR (Comiso bootstrap)	AMSR-E/AMSR2; 18.7 GHz (27 km x 16 km/ 22 km x 14 km), 36.5 GHz (14 km x 8 km/ 12 km x 7 km)	25 km x 25 km PolarStereo	Comiso et al., 2003; Comiso and Nishio, 2008; Comiso, 2009
ASI-SSMI (ASI)	SSM/I, SSMIS; 85.5 GHz (15 km x 13 km)	12.5 km x 12.5 km PolarStereo	Kaleschke et al., 2001; Ezraty et al., 2007
NT1-SSMI (NASA-Team)	SSM/I, SSMIS; 19.35 GHz (69 km x 43 km), 37.0 GHz (37 km x 28 km)	25 km x 25 km PolarStereo	Cavalieri et al., 1984; 1992; 1999
NT2-AMSR (NASA-Team-2)	AMSR-E/AMSR2; 18.7 GHz (27 km x 16 km/ 22 km x 14 km), 36.5 GHz (14 km x 8 km/ 12 km x 7 km), 89.0 GHz (6 km x 4 km/ 5 km x 3 km)	25 km x 25 km PolarStereo	Markus and Cavalieri, 2000; 2009

139

140 2.2 The Landsat data set

141 Landsat data of the Thematic Mapper TM on Landsat-5, the Enhanced Thematic Mapper (ETM) on Landsat-7, and
 142 Operational Land Imager (OLI) on Landsat-8 were obtained in Level 1c GeoTIFF format from <https://earthexplorer.usgs.gov>
 143 [last accessed: June 28, 2021] for years 2003-2011 (Landsat-5), 2003 (Landsat-7), and 2013-2015 (Landsat-8). Only images
 144 with a cloud fraction < 30 % provided as a search criterion upfront, were selected and downloaded from the server. In the
 145 Northern Hemisphere, we use images of months March, April, May and September, i.e. from late winter to spring and at the
 146 onset of fall freeze-up; in the Southern Hemisphere we use images of months October through March, i.e. from late winter
 147 over summer to fall freeze-up. The total number of images acquired is 421; these split into 152, 12, and 227 for Landsat-5, 7
 148 and 8, respectively, and partition into 259 images for the Northern Hemisphere and 162 images for the Southern Hemisphere.
 149



150 **2.2.1 Processing**

151 We compute the top of atmosphere (TOA) reflectance for channels 2 to 4 (Landsat-5 and 7) or channels 3 to 5
152 (Landsat-8) following Chander et al. (2007; 2009) and USGS (2015). Table 2 provides the wavelengths of the channels used
153 (e.g. Chander et al., 2009; Barsi et al., 2014). The solar zenith angle and other parameters required for this computation is
154 either included in the Landsat data files or is taken from Chander et al. (2007, 2009) and the Landsat 8 data users handbook
155 (USGS, 2015). To convert the TOA reflectances to surface reflectances or surface albedo we follow the approaches of Koepke
156 (1999) and Knap et al. (1999) that assume that the TOA reflectance (or planetary reflectance) equals the TOA albedo (or
157 planetary albedo) and that the TOA albedo α_{TOA} is related to the surface albedo $\alpha_{surface}$ via the simple linear relationship:

$$\alpha_{TOA} = a + b\alpha_{surface} \quad (1)$$

158 The coefficients a and b are a function of the atmospheric conditions, the solar zenith angle, and the wavelength. We follow
159 Koepke (1999) and take values for a and b from his figure 1 (KF1) and figure 2 (KF2). KF1 derived for the Advanced Very
160 High Resolution Radiometer (AVHRR) channel 1 we use for Landsat channels in the wavelength range 500-700 nm. KF2
161 derived for AVHRR channel 2 we use for Landsat channels in the wavelength range 700-900 nm. We choose those atmospheric
162 conditions that are appropriate for a polar marine atmosphere. For aerosol optical depth we use 0.05, for ozone content we use
163 0.24 cm[NTP] (NTP stands for normal temperature and pressure) corresponding to 240 Dobson Units, and for water vapor
164 content we used 0.5 g/cm². Using Eq. (1) we convert TOA albedo into surface albedo values separately for the three channels
165 of the respective Landsat instrument. Subsequently, we compute from these surface albedo values an estimate of the surface
166 broadband shortwave albedo (e.g. Brandt et al., 2005) using the bandwidths of the channels as weights. The change in
167 bandwidths between the Landsat instruments is thus taken into account (see Table 2).
168
169

170 **Table 2.** Overview about the wavelengths of the Landsat channels used.
171

Wavelength [nm] of	Landsat-5	Landsat-7	Landsat-8
Channel 2	528-609	519-601	--
Channel 3	626-693	631-692	533-590
Channel 4	776-904	772-898	636-673
Channel 5	--	--	851-879

172 For every broadband surface albedo map, we perform a supervised visual classification into open water, bare / thin
173 ice and snow covered / thick ice. For that, we assume the respective surface class covers a Landsat pixel entirely. We assign
174 all dark pixels (with an albedo of, on average, smaller than 0.06) to the open water class. We assign all bright pixels (with an
175 albedo of, on average, larger than 0.45) to the class snow covered / thick ice; all remaining pixels fall into the class bare / thin
176 ice. We pay more attention separating open water from ice very accurately than to distinguish between bare / thin ice and
177 snow-covered / thick ice. In every Landsat albedo map we search for leads or openings, zoom into these and perform histogram-
178 equalized slicing to visually identify – based on albedo values and spatial structures – whether the leads or openings selected
179 contain open water. The threshold value chosen to separate open water from ice we take from Pegau and Paulsen (2001). The
180 threshold value chosen to distinguish between bare / thin ice and snow covered / thick ice is based on Brandt et al. (2005) and
181 Zatkan and Warren (2015). They found an albedo of around 0.33 for bare thin ice less than 30 cm thick and of around 0.42 for
182 snow covered thin ice (5 - 10 cm thick) with a thin (< 3 cm) snow cover. Note that the actual threshold values chosen for a
183 particular Landsat image varies between 0.03 and 0.08 for the open water – ice discrimination and between 0.35 and 0.55 for
184 the bare / thin ice – snow covered / thick ice discrimination. This variation results from the varying illumination conditions
185 encountered – despite our limitation to Landsat scenes acquired at solar zenith angles < 65°.
186

187 Usage of a three-class distribution is motivated by the fact that it has been shown that PMW SIC is often biased low
188 over thin sea ice (e.g. Wensnahan et al., 1993; Cavalieri, 1994; Ivanova et al., 2015). Therefore, in addition to using the Landsat
189 images just for a high-resolution ice-water discrimination we also use them to derive the fraction of thin ice with the aim to
190 discuss differences between Landsat SIC and PMW SIC in the light of a potential impact by thin ice. However, we discarded



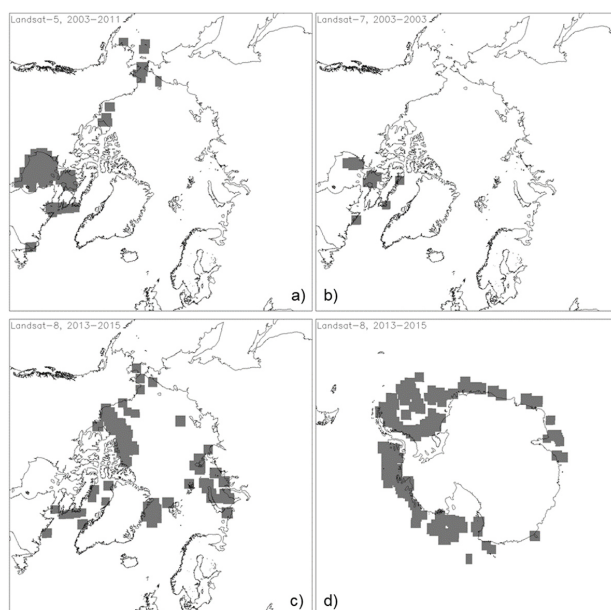
191 this aim – but kept the classification results – because during analyses of the Landsat images we encountered ambiguities in
192 surface albedos between snow-covered thin ice and bare thick ice. While there is little ambiguity between open water and ice,
193 except for very thin dark nilas or ice rind (e.g. Zatko and Warren, 2015), resulting in high confidence of pixels classified as
194 either open water or ice, the confidence of pixels classified as bare/thin or snow covered/thick ice is considerably worse.

195

196 2.2.2 Co-location and comparison

197 For the co-location, we first select a rectangular area within the PMW SIC grid, EASE-2 for the SICCI-2 and OSI-
198 450 products and polar-stereographic true at 70 degrees northern or southern latitude (known as NSIDC grid) for the other six
199 products, which encloses the Landsat SIC map. For this we take the geographic corner coordinates of the Landsat SIC map
200 (still at 30 m grid resolution), convert these into Cartesian Coordinates and find those PMW SIC grid cells which centers have
201 minimum distance (in meters) to these corner coordinates. Beforehand, we also convert PMW SIC grid cell coordinates into
202 Cartesian coordinates and rotate the grid for the Northern Hemisphere PMW SIC products on the NSIDC grid clockwise by
203 45 degrees; this is not required for the respective Southern Hemisphere PMW SIC products.

204



205

206 **Figure 1.** Location of the Landsat scenes used. Panels a) through c) Arctic; panel d) Antarctic. Note that scenes do overlap.
207 The total number of scenes shown is 134 (a), 12 (b), 88 (c), and 134 (d).

208

209 Subsequently, we compute the Landsat SIC by summing over all 30 m pixels classified as ice that fall into the PMW
210 SIC grid cells within the above-defined rectangular area. Because we do this is at the grid resolution of the PMW products, we
211 obtain Landsat SIC maps at 12.5 km, 25.0 km, and 50.0 km grid resolution. We compare the resulting gridded Landsat SIC
212 with the respective co-located PMW SIC by computing the mean difference PMW SIC minus Landsat SIC and its standard
213 deviation, the median difference, and deriving a linear regression line and computing the linear correlation coefficient.

214

215 Based on a visual quality check of the obtained Landsat SIC maps we discard quite a number of processed Landsat
216 scenes from further analysis – mainly because of cloud artifacts but also because a few scenes we obtained twice. Therefore,
the final number of Landsat SIC maps used is lower than indicated above: 234 for the Arctic, partitioning into Landsat-5: 134,



217 Landsat-7: 12, and Landsat-8: 88, and 134 for the Antarctic. The spatial distribution of the Landsat scenes is illustrated in Fig.
 218 1. Note that we focus on data of Landsat-5 and Landsat-8 in this paper.

219

220 **2.2.3 Sensitivity analysis**

221 In order to estimate how Landsat SIC depends on the choice of the albedo thresholds used to discriminate open water
 222 from ice and bare / thin ice from snow covered / thick ice, we repeat the classification into the three surface classes using
 223 modified thresholds. We vary the albedo value for the open water – ice discrimination by ± 0.03 , i.e. for an actual albedo value
 224 of 0.06 we employ additional threshold values of 0.03 and 0.09. We vary the albedo value for the bare / thin ice – snow covered
 225 / thick ice discrimination by ± 0.1 , i.e. for an actual albedo value of 0.45 we employ additional threshold values of 0.35 and
 226 0.55. The range of albedo threshold values we choose is motivated by our experience with the supervised classification of the
 227 many Landsat scenes under varying illumination conditions. We arbitrarily select 12 Landsat 8 scenes for the Northern
 228 Hemisphere, and 15 scenes for the Southern Hemisphere. For every image we perform the classification into the three surface
 229 classes with the above-mentioned four additional albedo threshold value combinations, compute Landsat SIC on the 25 km
 230 and 50 km EASE grid and derive a Landsat scene mean SIC value (Tables 3 and 4). We find that changing the albedo value
 231 of the open water – ice discrimination by ± 0.03 changes the average Landsat SIC by between 0.7 % and 1.2 % in the Northern
 232 Hemisphere and by between 0.8 % and 1.5 % in the Southern Hemisphere. With that the sensitivity appears to be independent
 233 of the overall SIC which is close to 100 % for the Northern Hemisphere cases (Table 3) but 55 – 60 % for the Southern
 234 Hemisphere cases (Table 4). The difference in the sensitivity between grid resolutions of 25 km and 50 km is less than 0.2 %.

235
 236 **Table 3.** Landsat SIC derived using the actual pair of albedo threshold values (“Actual value”) and the four variations of them
 237 (see text) averaged for 12 Landsat-8 scenes selected for the Northern Hemisphere (NH) at 25 km and 50 km grid resolution.
 238 The number behind the \pm denotes one standard deviation. All SIC values are in percent.

$\alpha_{\text{thinice}} \setminus \alpha_{\text{openwater}}$	-0.03	Actual value	+0.03	NH, 25km
-0.1	99.2 \pm 2.1	--	97.3 \pm 3.7	
Actual value	--	98.0 \pm 3.1	--	
+0.1	99.2 \pm 2.1	--	97.3 \pm 3.7	
				NH, 50km
-0.1	98.9 \pm 3.2	--	96.9 \pm 4.5	
Actual value	--	97.7 \pm 4.1	--	
+0.1	98.9 \pm 3.2	--	96.9 \pm 4.5	

239

240 **Table 4.** Landsat SIC derived using the actual pair of albedo threshold values (“Actual value”) and the four variations of them
 241 (see text) averaged for 15 Landsat-8 scenes selected for the Southern Hemisphere (SH) at 25 km and 50 km grid resolution.
 242 The number behind the \pm denotes one standard deviation. All SIC values are in percent.

$\alpha_{\text{thinice}} \setminus \alpha_{\text{openwater}}$	-0.03	Actual value	+0.03	SH, 25km
-0.1	63.0 \pm 27.0	--	60.5 \pm 26.4	
Actual value	--	61.5 \pm 26.6	--	
+0.1	63.0 \pm 27.0	--	60.5 \pm 26.4	
				SH, 50km
-0.1	54.5 \pm 34.8	--	52.3 \pm 33.8	
Actual value	--	53.1 \pm 34.1	--	
+0.1	54.5 \pm 34.8	--	52.3 \pm 33.8	

243

244 As expected, changing the albedo value of the bare / thin ice – snow-covered / thick ice discrimination by ± 0.1 does not
 245 influence the Landsat SIC. However, it influences the Landsat SIC computed at the respective grid resolutions when using
 246 Landsat pixels classified as snow-covered / thick ice only (Tables S02 and S03 in the Supplementary Material). We find
 247 Landsat SIC of thick ice to vary by between 1.4 % and 2.4 % in the Northern Hemisphere and by between 2.1 % and 2.7 % in
 248 the Southern Hemisphere with little difference between the grid resolutions. For the Landsat scenes used in this sensitivity



249 study in the Northern Hemisphere, we find a difference of 4.8 % between the total SIC and the SIC of pixels classified as
250 snow-covered / thick ice; hence the average bare / thin ice SIC is 4.8 %. In the Southern Hemisphere, the average bare / thin
251 ice SIC is 8.8 % at 25 km grid resolution and 7.5 % at 50 km grid resolution (not shown).

252

253 **2.2.4 Potential biases in Landsat SIC**

254 In our approach, we assume either ice or water to cover a Landsat pixel (30 m x 30 m) entirely, not taking into account
255 that ice floes or leads / openings might be smaller than the pixel size, resulting in a mixed ocean-ice pixel. This can introduce
256 a positive bias in the Landsat SIC computed at the grid resolution of the PMW SIC products. For instance, for a Landsat pixel
257 covered just half by snow covered / thick sea ice, which exhibits a surface albedo of 0.8 under cold conditions, the resulting
258 pixel average albedo would be $0.5 \times 0.06 + 0.5 \times 0.8 = 0.43$. With that, such a pixel is classified as bare / thin ice and counts
259 as a pixel with 100 % instead of 50 % sea-ice concentration. Depending on the albedo of the ice, an ice-cover fraction of 0.04
260 in one Landsat pixel could be sufficient to increase the pixel average albedo above the upper open water – ice discrimination
261 threshold value of 0.09 (see Tables 3, 4), causing the respective pixel to be classified as 100 % ice.

262 In order to quantify this positive bias better, it is useful to distinguish between sea-ice conditions during summer and
263 winter, between pack ice and the MIZ, and to take into account the dimensions of leads / openings and ice floes. Distributions
264 of lead width and floe size both follow a power law. Leads / openings and ice floes with dimensions smaller than the Landsat
265 pixel size are orders of magnitude more abundant than wide leads / openings (e.g. Tschudi et al., 2002; Marcq and Weiss,
266 2012) and large ice floes (e.g. Steer et al., 2008; Toyota et al., 2011; Perovich and Jones, 2014).

267 Based on airborne digital camera visible imagery captured along several thousands' of kilometers long tracks of
268 Operation Icebridge (OIB) flights in the Arctic in April 2010 and in the Antarctic in October 2009 analyzed by Onana et al.
269 (2013) with respect to the lead and open water fraction, we find a SIC bias of less than 0.2 %. This value derived for an open
270 water fraction of ~ 1 % falls into the uncertainty range of our approach (see Tables 3, 4) and represents winter conditions in
271 the pack ice. Based on manual visual analysis of airborne visible imagery obtained in the MIZ in the Greenland Sea in March
272 1997, we find a SIC bias of the order of 5 to 10 %. This value is clearly outside the uncertainty range of our approach. The
273 images used here represent an ice cover of ~ 70 % SIC comprising closely packed but also broken bands of a few thicker ice
274 floes, pancake ice, brash and grease ice with little or no new ice formation in the openings – a typical situation at an ice edge
275 located in comparably warm water.

276 Next, we again take the results of Onana et al. (2013) but assume that the thin ice identified in the OIB digital camera
277 imagery adds to the open water fraction thereby simulating a summer situation. For an open water fraction of then ~ 5 %, we
278 estimate a SIC bias of less than 0.8 %, which is still within the uncertainty range of our approach. However, this low positive
279 bias during summer would only apply to a situation where ice floes are still packed closely together, e.g. by herding of ice
280 floes (e.g. Toyota et al., 2016), and where gaps between the ice floes from additional openings created by the melt process are
281 filled by brash ice and/or slush. While this is a situation that might be encountered during summer (Steer et al., 2008; Lu et al.,
282 2008), it is not necessarily typical. In summer, it can be more common to encounter isolated floes. Depending on the size of
283 the floes and their distribution across a 25 km grid cell with, e.g., 50 % SIC, we find the bias to range between less than 2 %
284 to 50 % in the two most extreme cases. We refer to the Supplementary Material to this subsection, where we describe in more
285 detail how we obtain estimates of the positive bias caused by the combination of i) the finite resolution of the Landsat sensor
286 and ii) our classification approach for both winter and summer conditions at the scale of a 25 km PMW SIC product grid.

287 According to the high-resolution optical images used to infer the floe size distribution (Steer et al., 2008; Toyota et
288 al., 2011; 2016) and similar studies (e.g. Paget et al., 2001; Lu et al., 2008; Zhang and Skjetne, 2015), the ice cover often
289 comprises a large spectrum of floes. The larger and largest floes at the upper end of the floe-size distribution form the major
290 fraction of the sea-ice area (in square kilometers) (e.g. Paget et al., 2001; Steer et al., 2008). A small number of large floes
291 results in a smaller number of mixed ocean-ice Landsat pixels than a large number of smaller floes. Hence, where larger floes



292 dominate our Landsat SIC estimate is less biased than where small floes dominate. The effect of the ocean swell, the
293 dominating force for fracturing ice floes according to, e.g., Toyota et al. (2016), is larger close to the ice edge than further
294 inside the ice pack. Therefore, a larger number of smaller floes exists along the ice edge, suggesting a larger bias in our Landsat
295 SIC near the ice edge than inside the ice pack. Without further independent information about the actual ice cover, we are not
296 able quantifying this bias accurately.

297 In summary, we state: for high-concentration winter conditions and for those cases during summer where ice floes
298 are closely packed and openings between the floes are covered with brash ice and slush, the bias in Landsat SIC derived at the
299 spatial scale of the PMW SIC products falls within the retrieval uncertainty range of our approach (see Tables 3, 4). The bias
300 could fall outside the uncertainty range near the ice edge during winter when sea ice drifts into comparably warm waters that
301 inhibit ice formation in newly created openings; here biases as high as 10 % in a single PMW grid cell could occur. The bias
302 could also fall outside the uncertainty range during summer; here biases between 5 % and 20 % in single PMW grid cells might
303 occur depending on proximity to the ice edge and hence floe-size distribution and depending on conditions favoring / inhibiting
304 herding of ice floes into bands.

305 **3 Results**

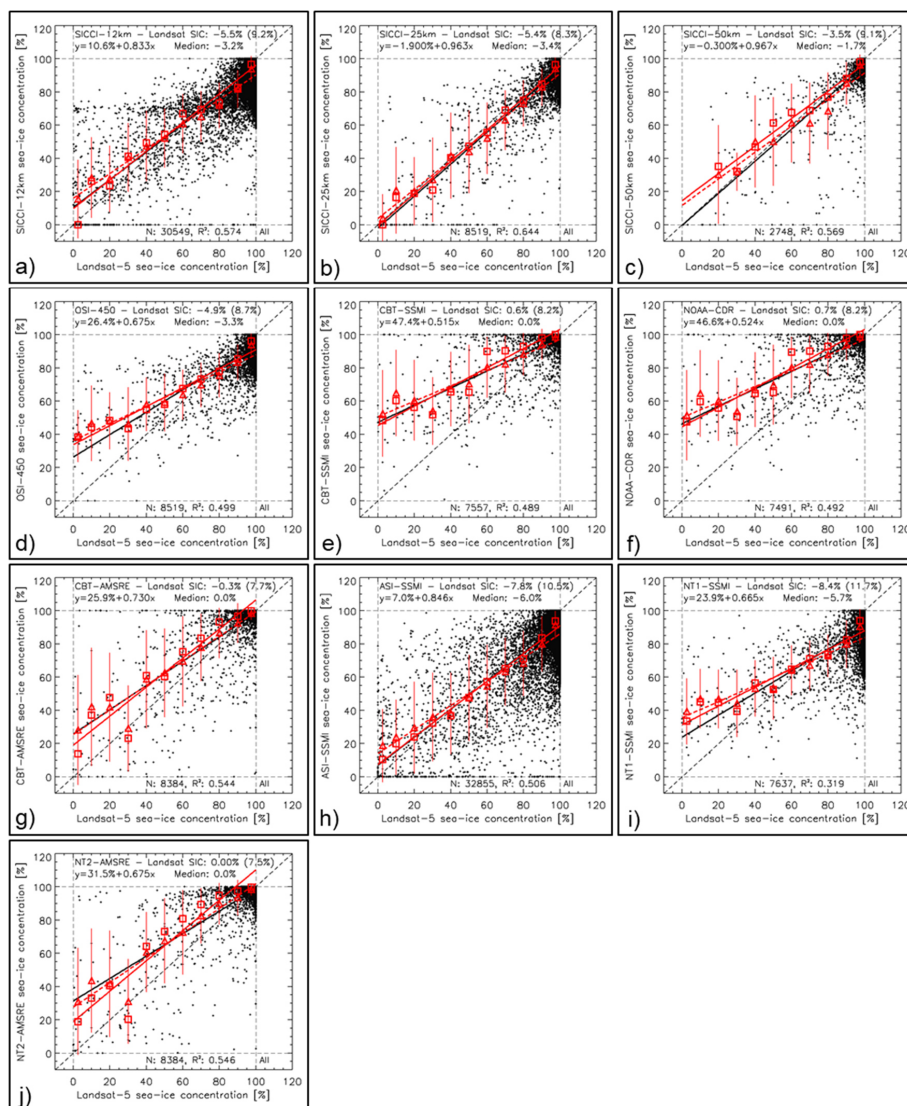
306 In the following, we present and discuss results obtained in the Northern and Southern Hemisphere. We preferred to
307 not merge the results of Landsat-5 and Landsat-8 in the Northern Hemisphere because with that we have a relatively natural
308 discrimination between cases dominated by first-year ice (Landsat-5) and cases dominated by mixed first-year / multiyear ice
309 or multiyear ice (Landsat-8) (see Fig. 1).

310 **3.1 Northern Hemisphere**

311 Out of the ten products, SICCI-25km, SICCI-50km, ASI-SSMI, and SICCI-12km offer the best linear agreement with
312 Landsat SIC for first-year ice dominated cases as expressed, e.g., by the location of mean and median PMW SIC (red symbols)
313 in Fig. 2 and the values of slope, intercept and correlation coefficient listed in Table 5. The two CBT products, NOAA-CDR
314 and NT2-AMSRE have the smallest overall mean difference and zero median (Table 5). These four products exhibit, however,
315 a considerable tail of near-100 % PMW SIC values stretching across almost the entire Landsat SIC range, pointing towards
316 over-estimation of Landsat SIC. ASI-SSMI and NT1-SSMI SIC spread towards comparably low values at high Landsat SIC,
317 i.e. along the vertical dashed line denoting 100 % Landsat SIC (Fig. 2 h, i) contributing to the overall largest underestimation
318 of Landsat SIC among the ten products (Table 5).

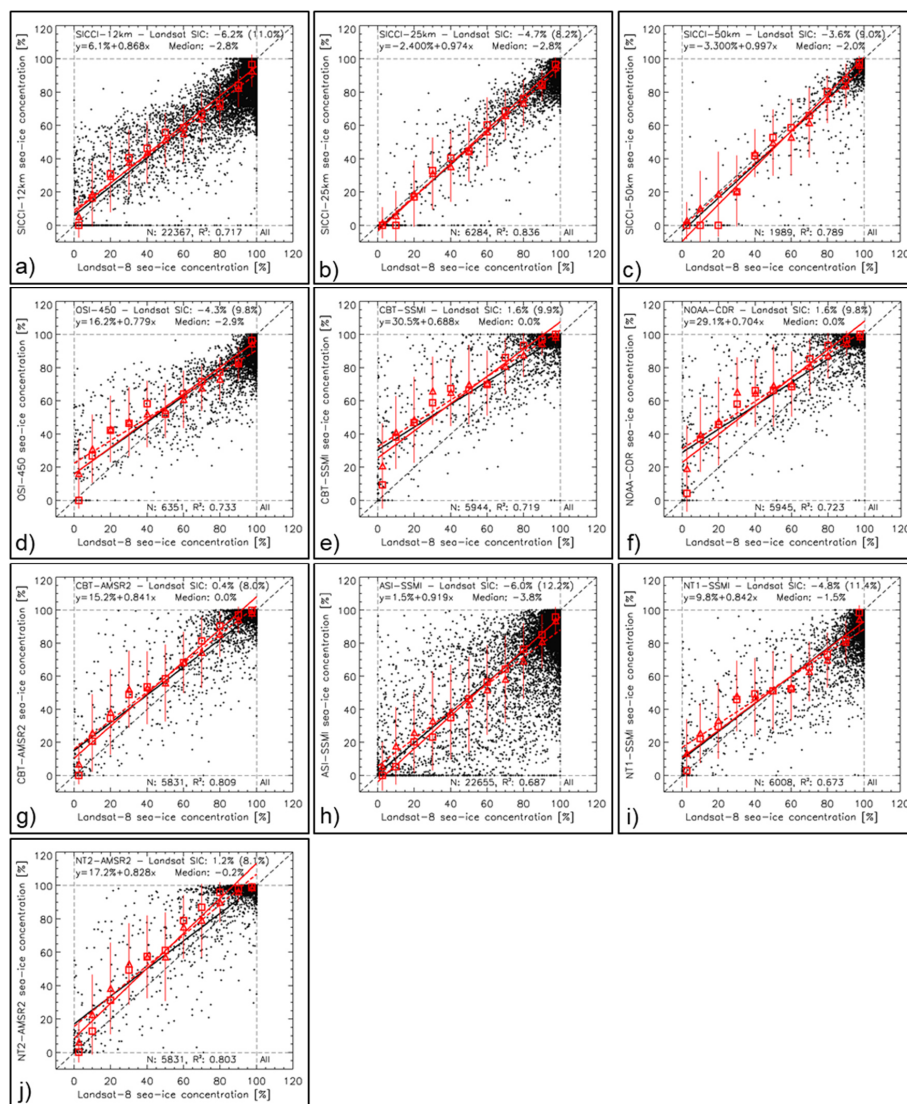
319 For cases with mixed first-year / multiyear or multiyear ice, SICCI-25km and SICCI-50km offer best linear agreement
320 with Landsat SIC in the Northern Hemisphere (Fig. 3). Most other products have a less convincing linear relationship with the
321 majority of the data pairs being located either above (NT2-AMSR2) or below (ASI-SSMI) the identity line or within a point
322 cloud across this line (SICCI-12km, OSI-450, NT1-SSMI). Like for first-year ice, the two CBT products, NOAA-CDR and
323 NT2-AMSR have the smallest mean difference for mixed first-year / multiyear or multiyear ice (Fig. 3, Table 6). However,
324 particularly at higher Landsat SIC these products show many data pairs above the identity line and the linear regressions
325 through the mean and median PMW SIC (red dashed and solid lines) are also located above the identity line – in contrast to,
326 e.g. SICCI-25km and SICCI-50km.

327



328
 329
 330
 331
 332
 333
 334
 335
 336
 337
 338
 339

Figure 2. Scatterplots of PMW SIC (y-axis) versus Landsat SIC (x-axis) for all ten products for the first-year ice dominated cases from 2003-2011 in the Northern Hemisphere (Landsat-5). Black dots are individual data pairs, the black solid line is the linear regression, and the black dashed line is the identity line. Red triangles denote the mean PMW SIC computed for Landsat SIC ranges 0%-5%, 5%-15%, 15%-25%, ..., 85%-95%, 95%-100%, red bars one standard deviation of these mean values and the red dashed line is the respective linear regression line. Red squares denote the median PMW SIC for the same Landsat SIC ranges and the red solid line is the respective linear regression line. The overall mean and median difference PMW SIC minus Landsat SIC, its standard deviation, and the equation of the linear regression through the individual data pairs is shown at the top, the number N of data pairs and the squared linear correlation coefficient at the bottom of each panel.



340

341 **Figure 3.** Scatterplots of PMW SIC (y-axis) versus Landsat SIC (x-axis) for all ten products for mixed first-year / multiyear
 342 or multiyear ice cases from 2013-2015 in the Northern Hemisphere (Landsat-8). See Fig. 2 for a description of symbols, lines
 343 and text.

344

345 The linear agreement between PMW SIC and Landsat SIC improves in general for all ten products for mixed first-
 346 year / multiyear or multiyear ice cases (Fig. 3, Table 6) compared to first-year ice (Fig. 2, Table 5). This improvement is
 347 comparably large for OSI-450: slope increases by ~0.10 and NT2-AMSR: slope increases by ~0.15 but quite small for SICCI-
 348 25km and SICCI-50km because slopes are close to unity already. Hence, despite the larger magnitude of overall mean and
 349 median SIC differences, of all ten products SICCI-25km and SICCI-50km provide the most stable linear agreement with
 350 Landsat SIC in the Northern Hemisphere. These two products provide SIC estimates for first-year ice which are almost as
 351 accurate as the SIC estimates for mixed first-year ice / multiyear ice or multiyear ice. This could be one consequence of the
 352 self-optimizing hybrid SICCI-2 / OSI-450 algorithm (Lavergne et al., 2019) and of the way ice tie points are chosen in
 353 comparison to the other products (e.g., Kern et al. 2020).



354 **Table 5.** Summary of the statistical parameters displayed in Fig. 2. Diff, DiffSDEV, and Median (all in percent SIC) are the
 355 mean difference PMW SIC minus Landsat SIC, its standard deviation and the median difference; Slope and Intercept (in
 356 percent SIC) are the coefficients of the linear regression, and R^2 and N are the squared linear correlation coefficient and number
 357 of data pairs, respectively. Numbers in **bold** and *bold italic* font denote the respective “best” and “2nd best” value, respectively,
 358 e.g. largest and 2nd-largest values of R^2 and lowest and 2nd-lowest values of Diff, Intercept and difference unity minus slope.
 359

LS5, NH 2003-11	SICCI- 12	SICCI- 25	SICCI- 50	OSI- 450	CBT- SSMI	NOAA- CDR	CBT- AMSRE	NT1- SSMI	ASI- SSMI	NT2- AMSRE
Diff	-5.5	-5.4	-3.5	-4.9	0.6	0.7	-0.3	-8.4	-7.8	0.0
DiffSDEV	9.2	8.3	9.1	8.7	8.2	8.2	7.7	11.7	10.5	7.5
Median	-3.2	-3.4	-1.7	-3.3	0.0	0.0	0.0	-5.7	-6.0	0.0
Slope	0.833	0.963	0.967	0.675	0.515	0.524	0.730	0.665	0.846	0.675
Intercept	10.6	-1.9	-0.3	26.4	47.4	46.6	25.9	23.9	7.0	31.5
R^2	0.57	0.64	0.57	0.50	0.49	0.49	0.54	0.32	0.51	0.55
N	30549	8519	2748	8519	7557	7491	8384	7637	32855	8384

360

361 **Table 6.** Summary of statistical parameters shown in Fig. 3. See Table 5 for an explanation of the parameters given.

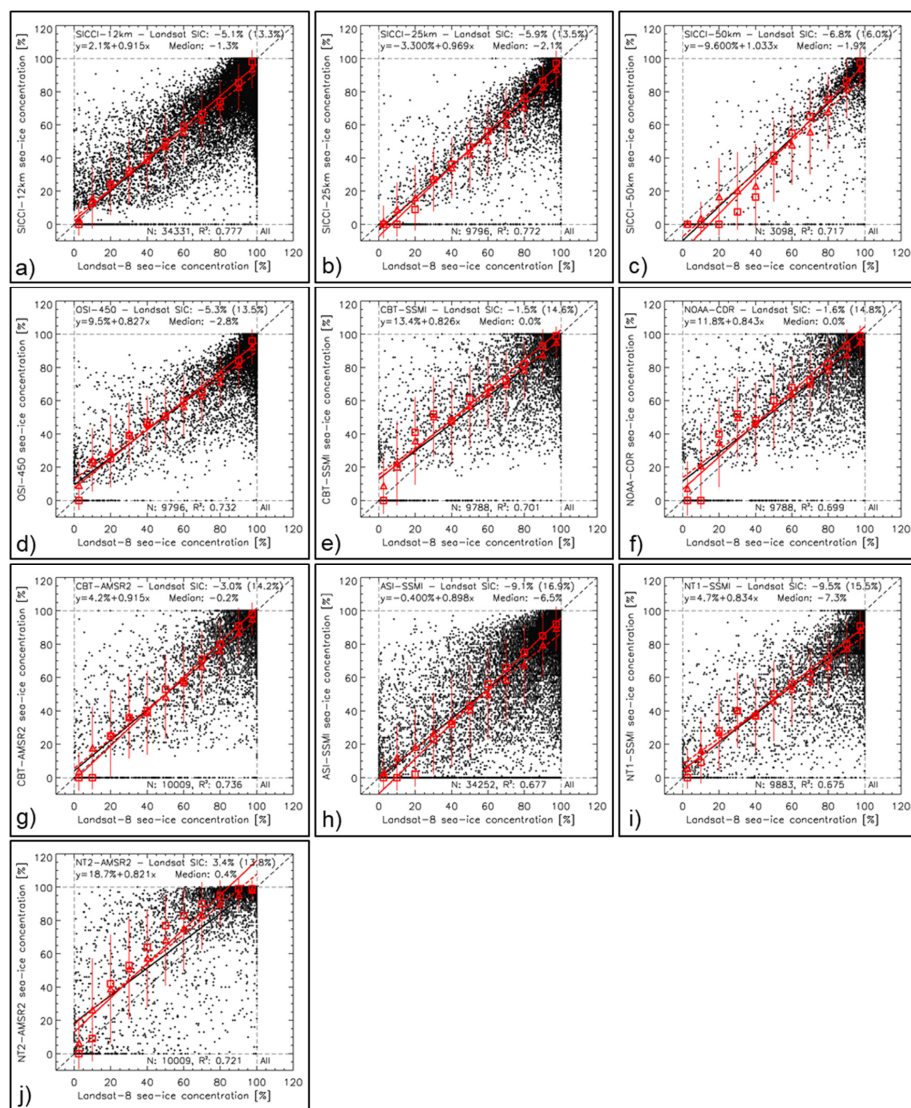
LS8, NH 2013-15	SICCI- 12	SICCI- 25	SICCI- 50	OSI- 450	CBT- SSMI	NOAA- CDR	CBT- AMSR2	NT1- SSMI	ASI- SSMI	NT2- AMSR2
Diff	-6.2	-4.7	-3.6	-4.3	1.6	1.6	0.4	-4.8	-6.0	1.2
DiffSDEV	11.0	8.2	9.0	9.8	9.9	9.8	8.0	11.4	12.2	8.1
Median	-2.8	-2.8	-2.0	-2.9	0.0	0.0	0.0	-1.5	-3.8	-1.5
Slope	0.868	0.974	0.997	0.779	0.688	0.704	0.841	0.842	0.919	0.828
Intercept	6.1	-2.4	-3.3	16.2	30.5	29.1	15.2	9.8	1.5	17.2
R^2	0.72	0.84	0.79	0.73	0.72	0.72	0.81	0.67	0.69	0.80
N	23433	6484	2056	6576	5944	5945	5831	6008	22655	5831

362

363 3.2 Southern Hemisphere

364 In the Southern Hemisphere, slope and location of the linear regression lines as well as of the mean and median PMW
 365 SIC values (red symbols) is more similar between the ten products (Fig. 4, Table 7). The linear agreement is fairly good for
 366 SICCI-2 products, CBT-AMSR2 and ASI-SSMI. Like in the Northern Hemisphere, SICCI-25km and SICCI-50 km reveal the
 367 best linear agreement with Landsat SIC but SICCI-50km appears to be negatively biased. This bias is associated with a large
 368 number of PMW SIC values of 0 % at non-zero Landsat SIC which is also reflected by the mean and median PMW SIC
 369 (compare Fig. 4c) with Fig. 3c). We discuss this issue and the observation that all products except CBT-SSMI, NOAA-CDR
 370 and CBT-AMSR2 exhibit SIC values below about 10-15 % while these three products lack values in the PMW SIC range
 371 between 0 % and ~15 % in Section 5.4.

372 Like in the Northern Hemisphere (Table 6), the magnitude of the SIC difference is smallest for NT2-AMSR2, NOAA-
 373 CDR and the two CBT products and largest for NT1-SSMI and ASI-SSMI. Of all ten products, NT2-AMSR2 (Fig. 4 j) offers
 374 the most asymmetric SIC distribution and a considerable overestimation of Landsat SIC in the range between ~40 % and ~90
 375 %, also expressed by median SIC > mean SIC for all Landsat SIC bins above 25 % (Fig. 4 j). NT2-AMSR2 is the only product
 376 with a substantial positive overall mean difference of 3.4 %, even the median difference is > 0 % (Table 7).



377
 378 **Figure 4.** Scatterplots of PMW SIC (y-axis) versus Landsat SIC (x-axis) for all ten products for 2013-2015 in the Southern
 379 Hemisphere. See Fig. 2 for a description of symbols, lines and text.

380
 381 **Table 7.** Summary of statistical parameters shown in Fig. 4. See Table 5 for an explanation of the parameters given.

LS8, SH 2013-15	SICCI- 12	SICCI- 25	SICCI- 50	OSI- 450	CBT- SSMI	NOAA- CDR	CBT- AMSR2	NT1- SSMI	ASI- SSMI	NT2- AMSR2
Diff	-5.1	-5.9	-6.8	-5.3	-1.5	-1.6	-3.0	-9.5	-9.1	3.4
DiffSDEV	13.3	13.5	16.0	13.5	14.6	14.8	14.2	15.5	16.9	13.8
Median	-1.3	-2.1	-1.9	-2.8	0.0	0.0	-0.2	-7.3	-6.5	0.4
Slope	0.915	0.969	1.033	0.827	0.826	0.843	0.915	0.834	0.898	0.821
Intercept	2.1	-3.3	-9.6	9.5	13.4	11.8	4.2	4.7	-0.4	18.7
R ²	0.78	0.77	0.72	0.73	0.70	0.70	0.74	0.68	0.68	0.72
N	34331	9796	3098	9796	9788	9788	10009	9883	34252	10009



383 **3.3 Hemispheric Similarities and Differences**

384 Overall, agreement between PMW SIC and Landsat SIC differs between the two hemispheres. For all products, we find
 385 a substantially larger scatter of SIC values around the identity line in the Southern Hemisphere (section 3.2) than the Northern
 386 Hemisphere (section 3.1). On the one hand, this larger scatter in the Southern Hemisphere could be the result of a considerably
 387 larger number of Landsat scenes of cases with low SIC, naturally resulting in a larger spread of the SIC. In addition, the
 388 majority of the Landsat scenes in the Southern Hemisphere reflect late spring / summer conditions. During such conditions,
 389 snow metamorphism due to melt and melt-refreeze cycles substantially change the sea ice surface emissivity on daily time-
 390 scales and sub grid-cell size spatial scales (e.g. Willmes et al., 2014) causing a larger scatter in SIC. On the other hand, we are
 391 dealing with an unknown amount of overestimation of the actual sea-ice concentration by our Landsat SIC during summer
 392 melt due to mixed ocean-ice Landsat pixels (Subsection 2.2.4). We refer to Sections 4.3, 5.1 and 5.2 for more discussion on
 393 this issue.

394 In general, we find the scatter is larger for products offered at finer grid resolution, e.g. SICCI-12km and ASI-SSMI,
 395 than for the coarser grid-resolution products. The larger number of valid SIC pairs of the high-resolution products result in
 396 more scatter due to the inherent retrieval noise – even though the capability to resolve smaller-scale SIC variations is better
 397 for the fine- than the coarser-resolution products (see section 5.1). In addition, a mismatch in the location of a, for example,
 398 10km-scale ice tongue between a Landsat scene and a PMW SIC product has a substantially larger influence on the SIC
 399 difference at 12.5 km than at 25 or 50 km grid resolution. The fact that oversampling is much larger at 12.5 km than at 50 km
 400 plays a role here also. Even using simulated brightness temperatures one gets a large spread between a reference SIC and the
 401 PMW SIC due to resolution mismatch (see e.g. Tonboe et al., 2016). Note in this context that we estimate Landsat SIC at the
 402 grid resolution of the respective products, i.e. 12.5 km, 25.0 km or 50.0 km.

403
 404 **Table 8.** Comparison of statistical parameters listed in Tables 5 and 6 in the Northern Hemisphere for SICCI-2 and OSI-450
 405 products using truncated or non-truncated (near-100 % SIC) PMW SIC data. See Table 5 for an explanation of the parameters
 406 given. Top (LS5, NH 2003-11) is for first-year ice dominated cases, bottom (LS8, NH 2013-15) is for mixed first-year /
 407 multiyear and multiyear ice cases. The overall median differences do not change and are not listed again.

LS5, NH 2003-11	SICCI-12	SICCI-12 non-truncated	SICCI-25	SICCI-25 non-truncated	SICCI-50	SICCI-50 non-truncated	OSI-450	OSI-450 non- truncated
Diff	-5.5	-4.6	-5.4	-5.0	-3.5	-3.0	-4.9	-4.5
DiffSDEV	9.2	10.0	8.3	8.7	9.1	9.3	8.7	9.0
Slope	0.833	0.852	0.963	0.974	0.967	0.979	0.675	0.684
Intercept	10.6	9.6	-1.9	-2.5	-0.3	-1.0	26.4	26.0
R ²	0.57	0.54	0.64	0.63	0.57	0.56	0.50	0.48
LS8, NH 2013-15								
Diff	-6.2	-4.9	-4.7	-4.4	-3.6	-3.4	-4.3	-3.9
DiffSDEV	11.0	12.1	8.2	8.5	9.0	9.1	9.8	9.9
Slope	0.868	0.891	0.974	0.982	0.997	1.000	0.779	0.786
Intercept	6.1	5.2	-2.4	-2.7	-3.3	-3.5	16.2	15.9
R ²	0.72	0.68	0.84	0.83	0.79	0.79	0.73	0.73

409
 410 SICCI-2 products and OSI-450 provide access to SIC values above 100 % and below 0 % that are naturally retrieved
 411 due to the brightness temperature distribution around ice and water tie points used. Kern et al. (2019) found that incorporation
 412 of these so-called off-range or non-truncated SIC values provides a more accurate estimate of accuracy, i.e. difference to the
 413 true SIC value, and precision, i.e. standard deviation of this difference. Table 8 reveals that independent of the ice type, the



414 magnitude of the mean difference decreases while the slope of the linear regression increases, becoming closer to unity, in
415 agreement to Kern et al. (2019). We observe the same in the Southern Hemisphere (Table S05 in the supplementary material).
416 Of particular interest in this regard are high-concentration cases discussed in more detail in Section 4.2 but also the effect of
417 the truncation at 0 % in the context of filters used to mitigate spurious SIC values (see Section 5.3).

418 4 Case Studies

419 In the previous section, we showed results independent of the ice regime (see below) – except for some general
420 discussion about the observed differences between cases with predominantly first-year ice (Landsat-5) and cases with a mixture
421 of first-year / multiyear or multiyear ice (Landsat-8). This section deals with our comparison between PMW SIC and Landsat
422 SIC for the following ice regimes: “ice edge”, “leads and openings” = cases with leads and coastal polynyas or openings,
423 “heterogeneous ice” = cases with irregularly shaped openings in the ice pack, “freeze-up”, “high-concentration ice”, and “melt
424 conditions” (see Table S01 in the supplementary material). We show in more detail results of the last three ice regimes known
425 to cause biases in PMW SIC products. For all remaining regimes we show examples in Figs. S04 through S09 in the
426 supplementary material while the results of the statistical comparison for all regimes will be summarized in Figs 10 and 11.

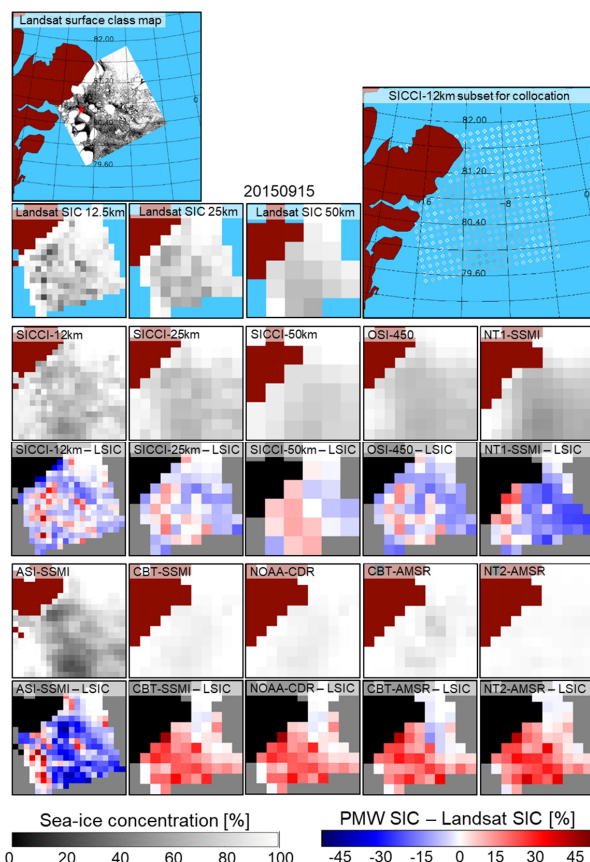
427 4.1 Freeze-Up

428 These are cases where according to the date, geographic location and information in the Landsat scene freeze-up has
429 commenced. We select Landsat scenes containing a considerable fraction of new and thin ice; these are acquired in September
430 and February/March in the Northern and Southern Hemisphere, respectively. We have got only few such cases in both
431 hemispheres (see Table S01 in the supplementary material). We expect PMW SIC underestimates Landsat SIC (LSIC) –
432 particularly for young and thin ice with a thickness < 0.2 m (e.g. Ivanova et al., 2015). Figure 5 illustrates the conditions for a
433 Landsat-8 scene close to Greenland in the Fram Strait on September 15 2015. The classified Landsat-8 image (Fig. 5, top left)
434 reveals a mix of large ice floes – presumably second-year or older ice – and meandering patches of smaller floes embedded
435 into a matrix of mostly grey and a few dark pixels; the grey pixels are supposed to represent bare / thin sea ice, the dark pixels
436 open water. All products agree well with Landsat SIC in the topmost part of the scene over high-concentration ice. PMW SIC
437 maps of six of the ten products (SICCI-2 products, OSI-450, NT1-SSMI and ASI-SSMI) reveal an overall SIC distribution
438 similar to Landsat SIC. For the remaining four products, the SIC difference maps show widespread overestimation of LSIC by
439 PMW SIC expressed by positive (red) values. Unlike expected, we do not observe negative SIC differences for the entire
440 greyish area of the Landsat-8 scene.

441 The main reason for this observation is the actual ice condition. Very likely the greyish area represents a mixture of
442 sub-pixel size, i.e. less than 30 m x 30 m, ice floes and brash ice formed from disintegrated thicker ice floes and young / new
443 sea ice. On the one hand, the sub-pixel size floes and the brash ice are thicker than young / new sea ice. These forms of sea ice
444 exhibit different surface properties and hence microwave emissivity than young / new thin sea ice. For such a mixture of ice
445 types, it is particularly difficult to retrieve an accurate SIC with any of the algorithms used in the ten products. Ice tie points
446 do not adequately represent these ice conditions. On the other hand, for the greyish area the Landsat SIC could likely be too
447 high because of mixed ocean-ice Landsat pixels (see Subsection 2.2.4 and the respective supplementary material). Hence, what
448 appears to be 100 % thin ice might be just 50 % thick ice. However, observations conducted at Henrik Krøyer Holme station
449 (80°38'N 13°43'W, see star in Fig. 5, top left panel) on September 15 2015 and the preceding days indicate freezing conditions
450 with air temperatures between -5°C and -13°C (<https://www.dmk.dk/vejarkiv>, last access: June 29 2021). Therefore, it is quite
451 likely, new / thin ice covers most open water patches and any over-estimation of Landsat SIC due to sub-pixel size open water



452 patches is rather small. Therefore, to our opinion, the observed differences PMW SIC minus Landsat SIC are mainly caused
 453 by the above-mentioned difficulties of the PMW SIC algorithms to handle the complex sea-ice conditions encountered.
 454



455
 456 **Figure 5.** Landsat SIC, PMW SIC, and the difference PMW SIC minus Landsat SIC (LSIC) for all ten products for a freeze-
 457 up scene in the Fram Strait on September 15, 2015. The Landsat surface class map at the top left shows white: thick / snow-
 458 covered ice; grey: bare / thin ice; black: open water). The red star marks the location of Henrik Krøyer Holme station (see
 459 text). White and grey pixels are used to compute maps of gridded LSIC at 12.5 km, 25 km and 50 km, respectively (blue:
 460 outside Landsat image). A subset of SICCI-12km SIC grid cells shown at the top right illustrates the array used for the
 461 collocation. Panels in the remaining four rows show PMW SIC and PMW SIC minus LSIC for all ten products. Land is flagged
 462 brown in the SIC panels and black in the SIC difference panels; it differs between the PMW products. The land masks in the
 463 two bigger maps at the top come from the plotting routine used. LSIC maps use the land masks of the SICCI-2 products.

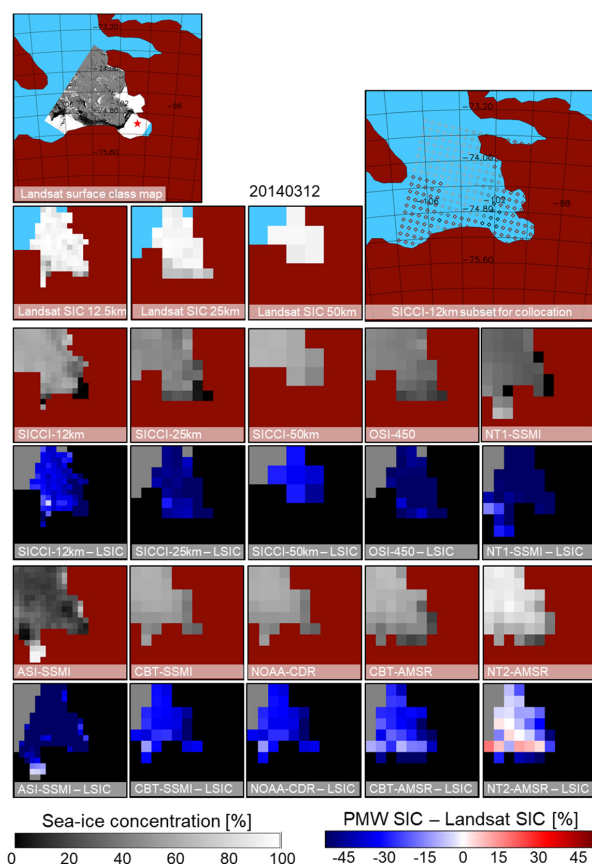
464
 465 Figure 6 illustrates a freeze-up case in Pine Island Bay, Amundsen Sea, Southern Ocean, on March 12, 2014. The
 466 classified Landsat-8 scene features a predominant coverage with new / young ice, some open water towards the coast and little
 467 thick / snow covered ice and icebergs in the open bay. Landsat SIC is mostly around 90 %; only few grid cells with low SIC
 468 exist close to the coast at 12.5 km and 25 km grid resolution. Nine of the ten PMW SIC products reveal considerably lower
 469 SIC values with SICCI-25km, OSI-450, NT1-SSMI and ASI-SSMI exhibiting particularly large widespread negative
 470 differences with magnitude > 40 %. An exception is NT2-AMSR2 exhibiting the highest PMW SIC of all ten products and



471 overall the smallest differences. It is the only product, though, which also exhibits positive differences, i.e. an over-estimation
 472 of Landsat SIC by up to 20 %.

473 The widespread under-estimation of Landsat SIC by almost all products is very well in line with the findings of
 474 Ivanova et al. (2015), albeit a bit large in magnitude. The new ice encountered in our example comprises a comparably large
 475 fraction of frazil / grease / small pancake ice while compared to nilas and grey/grey-white ice in Ivanova et al. (2015). Because
 476 Pine Island Glacier Automatic Weather Station (see star in top left map of Fig. 6) reported air temperatures between -11°C and
 477 -21°C on March 12, 2014 and the three preceding days (Mojica Moncada et al., 2019), the grey pixels in this Landsat scene
 478 very likely represent new/thin sea ice formed locally. However, we cannot fully exclude an over-estimation of Landsat SIC by
 479 sub-pixel size open water patches between streaks of new ice formed being classified as thin ice instead of open water (see
 480 Subsection 2.2.4 and respective supplementary material); for the conditions encountered this positive bias in Landsat SIC
 481 should be less than 5 %, maximum 10 %. The existence of such a positive bias combined with the different ice type encountered
 482 compared to Ivanova et al. (2015) explains why the observed under-estimation of Landsat SIC for most of the PMW SIC
 483 products is larger in magnitude than expected.

484



485

486 **Figure 6.** Landsat SIC, PMW SIC, and the difference PMW SIC minus Landsat SIC for all ten products for a scene near the
 487 coast during freeze-up in Pine Island Bay, Amundsen Sea, Southern Ocean, on March 12, 2014. The red star in the top left
 488 map marks the location of the Pine Island Glacier Automatic Weather Station (see text). Some of the white patches near the
 489 coast in this map are actually glacier ice not adequately flagged by the land mask. See Fig. 5 for more details.

490



491 Table 9 summarizes our results of the freeze-up cases for which we expected, overall, an under-estimation of Landsat
 492 SIC, i.e. a negative bias, due to a notable fraction of new / thin ice (see Ivanova et al., 2015). In the Northern Hemisphere,
 493 performance of the products differs a lot. We find positive biases for the two CBT-products, NOAA-CDR and NT2-AMSR2,
 494 large negative biases for the remaining products. SICCI-25km offers the best linear agreement with Landsat SIC. In the
 495 Southern Hemisphere, a number of products have a regression line slope close to unity, a small intercept and a squared linear
 496 correlation coefficient > 0.8. Most importantly, however, all products – except NT2-AMSR2 – on average under-estimate
 497 Landsat SIC in agreement with Ivanova et al. (2015).

498

499 **Table 9.** Summary of statistical results obtained for three freeze-up cases in the Northern Hemisphere (NH) and for 11 freeze-
 500 up cases in the Southern Hemisphere (SH) using Landsat 8 data. See Table 5 for an explanation of the parameters given.

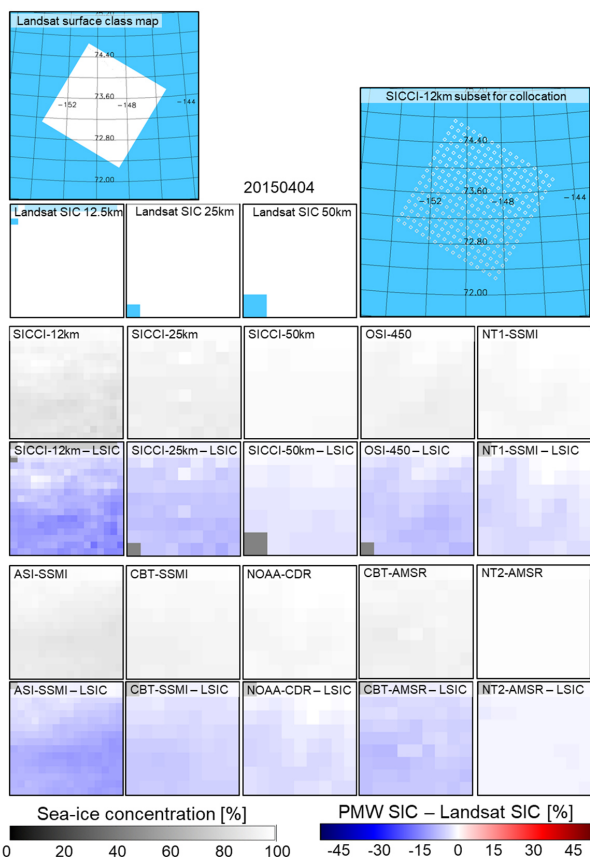
NH	SICCI-12	SICCI-25	SICCI-50	OSI-450	CBT-SSMI	NOAA-CDR	CBT-AMSR2	NT1-SSMI	ASI-SSMI	NT2-AMSR2
Diff	-8.2	-8.9	-10.5	-7.7	5.0	4.6	2.6	-14.1	-12.0	4.3
Diff SDEV	13.5	10.8	17.8	13.9	18.5	18.4	12.9	20.8	21.9	13.8
Slope	0.799	0.960	0.948	0.665	0.655	0.679	0.881	0.673	0.738	0.866
Intercept	7.8	-5.7	-6.4	19.3	31.6	29.4	12.0	11.3	8.6	14.9
R ²	0.77	0.84	0.65	0.70	0.58	0.58	0.77	0.50	0.51	0.74
N	751	208	64	210	191	191	186	196	702	186
SH										
Diff	-11.8	-12.1	-7.4	-12.1	-6.3	-6.1	-6.5	-10.9	-11.4	2.1
Diff SDEV	18.1	15.9	16.1	15.1	12.1	12.1	11.8	15.3	18.1	10.6
Slope	0.839	0.915	1.027	0.861	0.965	0.971	0.977	0.953	0.982	0.943
Intercept	2.0	-4.8	-9.7	0.1	-3.3	-3.7	-4.5	-6.9	-9.8	7.0
R ²	0.66	0.72	0.75	0.73	0.83	0.84	0.84	0.75	0.72	0.86
N	1843	531	169	531	536	536	547	540	1842	547

501 4.2 High-concentration ice

502 These are cases where the Landsat scene indicates either a closed ice cover without any leads or openings or an almost
 503 closed ice cover with few refrozen leads or openings, resulting in near-100 % Landsat SIC. In the ideal case, we expect PMW
 504 SIC is close to 100 %. Figure 7 illustrates such a case for April 4, 2015 in the Beaufort Sea, Arctic Ocean. Landsat SIC is
 505 100.0 %. All ten PMW SIC products exhibit quite high sea-ice concentrations – particularly SICCI-50km, NOAA-CDR and
 506 NT2-AMSR2. However, the difference maps clearly reveal a (very) small and negative bias for all PMW products. This bias
 507 is largest in magnitude for SICCI-12km and ASI-SSMI and smallest in magnitude for NT2-AMSR2.

508 Table 10 summarizes the results obtained for, in total, 40 high-concentration cases in the Northern Hemisphere: 28
 509 first-year ice dominated scenes (Landsat-5) and 12 scenes of mixed first-year / multiyear or multiyear ice cases (Landsat-8).
 510 We find the largest biases for SICCI-12km and ASI-SSMI independent of ice type. Except for CBT-AMSR and NT2-AMSR,
 511 all products exhibit a larger bias for first-year ice cases than mixed first-year / multiyear or multiyear ice cases. We hypothesize
 512 that the different biases between PMW and Landsat SIC for these near-100 % cases are caused by the different capabilities of
 513 the respective algorithms to derive an accurate SIC independent of ice type – as stated already in Section 3.1. NT1-SSMI and
 514 ASI-SSMI appear to have the largest difficulties with the different ice types encountered because their biases vary most. We
 515 note the two CBT products and NOAA-CDR (and NT2-AMSR2) have a median difference of 0.0 % independent of ice type
 516 – similar to Tables 5 and 6. For SICCI-2 products and OSI-450, median differences are smaller in magnitude than for all ice
 517 and approach zero for the mixed first-year / multiyear or multiyear ice cases.

518



519

520 **Figure 7.** Landsat SIC, PMW SIC, and the difference PMW SIC minus Landsat SIC for all ten products for a high-
 521 concentration scene in the Beaufort Sea, Arctic Ocean, on April 4, 2015. See Fig. 5 for a description of the maps shown.

522

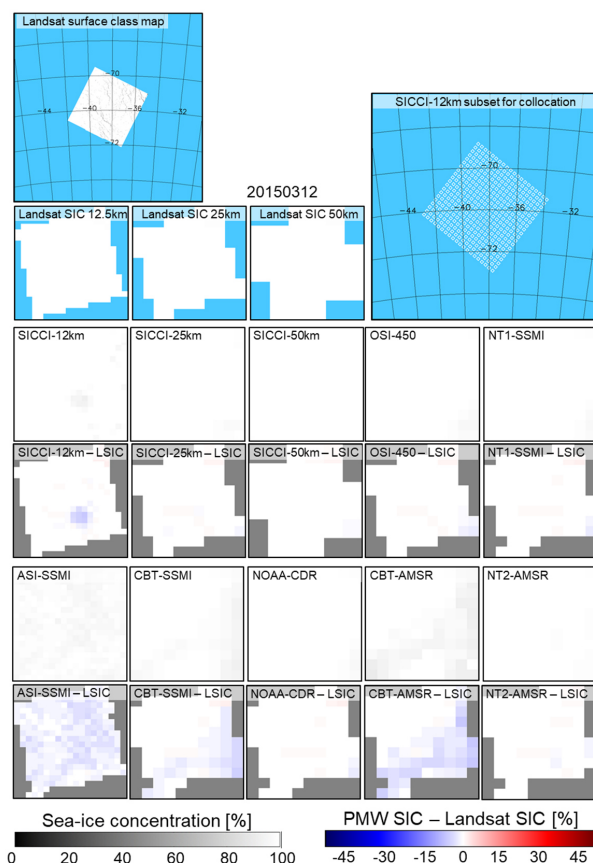
523 **Table 10.** Summary of statistical results obtained in the Northern Hemisphere for 28 cases with first-year ice (top, LS5, NH
 524 2003-11) and for 12 cases with mixed first-year / multiyear or multiyear ice (bottom, LS8, NH 2013-15). See Table 5 for an
 525 explanation of the parameters shown. For SICCI-2 and OSI-450 products, we include in all rows but “N” behind the “/” values
 526 based on non-truncated (near 100 %) SIC data. We omit slope and intercept because SIC data pairs cluster at 100 % and do
 527 not allow a meaningful estimation of a linear regression line.

LS5, NH 2003-11	SICCI-12	SICCI-25	SICCI-50	OSI-450	CBT-SSMI	NOAA-CDR	CBT-AMSR	NT1-SSMI	ASI-SSMI	NT2-AMSR
Diff	-4.0 / -3.0	-3.7 / -3.4	-1.5 / -1.0	-3.5 / -3.2	-0.8	-0.7	-0.9	-5.8	-6.9	-0.6
DiffSDEV	5.2 / 6.0	4.0 / 4.4	1.8 / 2.5	3.7 / 4.1	1.6	1.4	1.8	6.6	5.6	1.4
Median	-2.6 / -2.6	-2.5 / -2.5	-1.0 / -1.0	-2.4 / -2.4	0.0	0.0	0.0	-3.5	-6.0	0.0
N	7028	1978	677	1978	1940	1940	2104	1940	7633	2104
LS8, NH 2013-15										
Diff	-2.9 / -0.8	-1.5 / -0.5	-0.9 / -0.4	-1.3 / -0.3	-0.5	-0.2	-1.0	-0.3	-2.6	-0.6
DiffSDEV	4.1 / 6.2	2.2 / 3.1	1.2 / 1.7	1.9 / 3.0	1.4	0.9	3.0	0.9	2.6	2.5
Median	-0.2 / -0.2	-0.2 / -0.2	-0.3 / -0.3	-0.2 / -0.2	0.0	0.0	0.0	0.0	-2.1	-0.5
N	2659	764	242	764	714	714	723	714	2571	723

528



529 Using non-truncated SIC of SICCI-2 products and OSI-450 (see also Table 8), reduces the magnitude of the bias by
 530 between 0.5 % for SICCI-50km and 2.1 % for SICCI-12km for the mixed first-year / multiyear or multiyear ice cases (LS8)
 531 and less than that for the first-year ice cases. As expected, the standard deviation of the bias increases using non-truncated SIC.
 532 The other six PMW products set SIC values > 100 % to 100 % or do not permit a simple retrieval of such SIC values (NT2-
 533 AMSR2, but see Ivanova et al., 2015), and would therefore have a different bias and a larger standard deviation than shown in
 534 Table 10 (see Kern et al., 2019). Of the SICCI-2 / OSI-450 products, SICCI-50km provides the smallest bias and the smallest
 535 standard deviation of this bias: $-0.7 \% \pm 2.2 \%$ in line with Kern et al. (2019) who reported a bias of $-0.5 \% \pm 2.1 \%$ for non-
 536 truncated SICCI-50km SIC. The median difference of SICCI-2 products and OSI-450 is quite similar to the mean difference
 537 using non-truncated SIC for mixed first-year / multiyear or multiyear ice cases.



538

539 **Figure 8.** Landsat SIC, PMW SIC, and the difference PMW SIC minus Landsat SIC for all ten products for a high-
 540 concentration scene in the Weddell Sea, Southern Ocean, on March 12, 2015. See Fig. 5 for a description of the maps shown.
 541

542 Figure 8 illustrates a high-concentration case in the Weddell Sea, Southern Ocean, on March 12, 2015. Six of the ten
 543 PMW SIC products show almost 100 % sea-ice concentration and almost zero bias. We only find notable deviations from 100
 544 % concomitant with a small negative bias for ASI-SSMI, the two CBT-products and SICCI-12km. For our four high-
 545 concentration cases in the Southern Ocean (Table 11), we find the largest overall bias for ASI-SSMI. Most products reveal a
 546 bias of magnitude 0.3 % or smaller.



547 Using non-truncated SICCI-2 and OSI-450 SIC results in positive biases, ranging between 1.8 % for OSI-450 and 2.7
 548 % for SICCI-50km (Table 11, values behind the “/”). This amounts to an increase of the mean SICCI-2 / OSI-450 SIC for
 549 these cases by ~ 2.5 %. This increase is larger than in the Northern Hemisphere (compare Table 10). We explain this with a
 550 comparably large fraction of PMW SIC > 100 % for our small high-concentration cases data set of the Southern Hemisphere
 551 (four) compared to the Northern Hemisphere (40 in total). This is confirmed by median differences increasing from near-0 %
 552 to about the value of the mean differences using non-truncated SIC (Table 11).

553 Three of the four high-concentration cases identified in the Southern Ocean are from months November / December,
 554 a time of the year when melt onset and melt-refreeze cycles cause higher variability of the ice emissivity. One of the likely
 555 impacts is a notable fraction of PMW SIC > 100 % (see Fig. S01 in the supplementary material). The same applies in a different
 556 way to the case shown in Fig. 8, the only late fall / early winter case out of these four cases. The overall Landsat SIC of this
 557 scene is 99.9 %; that of an adjacent scene is 98.9 % (not shown). Sea ice and snow properties in late fall / early winter are often
 558 as well quite variable and can cause an elevated spread of the retrieved PMW SIC around 100 %, resulting in a substantial
 559 fraction of SIC values > 100 %. For instance, the overall SICCI-25km SIC is 101.9 % for the scene shown in Fig. 8 and 103.1
 560 % for the adjacent scene (not shown).

561

562 **Table 11.** Summary of statistical results obtained for the four high concentration cases in the Southern Hemisphere. See Table
 563 5 for an explanation of the parameters shown. For SICCI-2 and OSI-450 products, we include in rows “Diff”, “DiffSDEV”,
 564 and “Median” behind the “/” values obtained using non-truncated SIC.

LS8, SH 2013-15	SICCI-12	SICCI-25	SICCI-50	OSI-450	CBT-SSMI	NOAA-CDR	CBT-AMSR2	NT1-SSMI	ASI-SSMI	NT2-AMSR2
Diff	-0.1 / 2.5	0.0 / 2.4	0.0 / 2.7	-0.3 / 1.8	-0.7	0.1	-1.1	-0.9	-2.9	-0.1
DiffSDEV	1.7 / 2.9	0.8 / 2.3	1.2 / 2.7	2.1 / 3.1	1.7	0.7	2.0	2.6	2.5	1.2
Median	0.0 / 2.8	0.0 / 2.5	0.1 / 2.6	0.0 / 2.2	0.0	0.1	0.0	0.0	-2.4	0.0
N	978	287	93	287	288	288	302	288	973	302

565

566 4.3 Melt conditions

567 For melt-condition cases, we select Landsat scenes by means of the calendar date. In the Northern Hemisphere, we
 568 consider the time-period May 15 to May 31, in the Southern Hemisphere we used the time-period November 15 to February
 569 28. We did not include Landsat scenes subject to melt ponding on sea ice, e.g. during months June through August; this topic
 570 is covered in Kern et al. (2020).

571

572 **Table 12.** Summary of statistical results obtained for 15 melt-condition cases (without melt-ponds) in the Northern
 573 Hemisphere. See Table 5 for an explanation of the parameters shown. Numbers added behind the “/” for SICCI-2 and OSI-
 574 450 products denote the results obtained using non-truncated SIC.

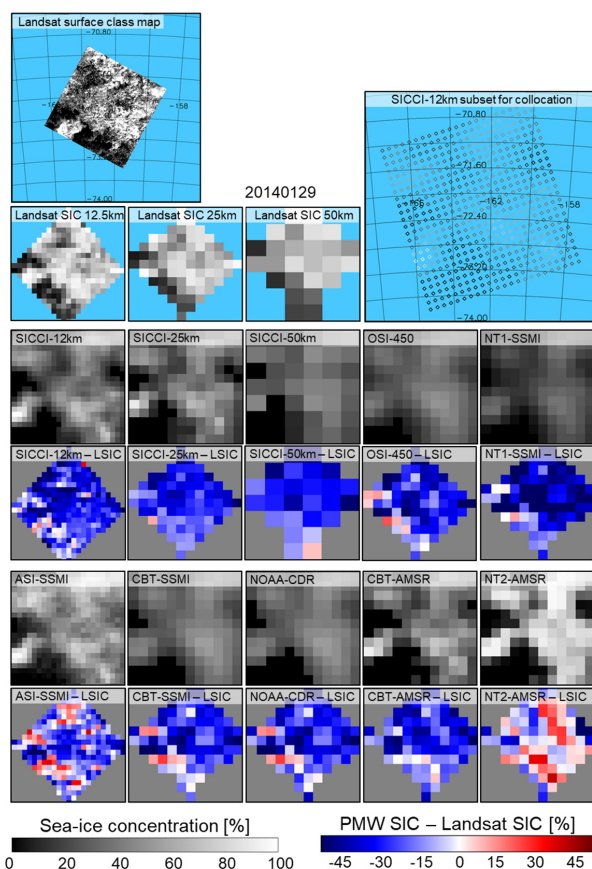
LS8, NH 2013-15	SICCI-12	SICCI-25	SICCI-50	OSI-450	CBT-SSMI	NOAA-CDR	CBT-AMSR2	NT1-SSMI	ASI-SSMI	NT2-AMSR2
Diff	-5.3 / -4.3	-5.1 / -4.6	-4.2 / -4.2	-4.6 / -4.3	2.2	2.4	0.2	-3.5	-4.7	1.7
DiffSDEV	10.5 / 11.2	8.9 / 9.3	9.6 / 9.6	9.5 / 9.7	9.8	9.7	7.4	10.8	12.2	8.3
Slope	0.829/0.852	0.930/0.943	0.898/0.899	0.617/0.626	0.418	0.416	0.727	0.637	0.740	0.564
Intercept	10.5 / 9.4	1.4 / 0.6	5.3 / 5.2	30.9 / 30.4	56.9	57.3	26.1	30.6	19.5	43.0
R ²	0.67 / 0.65	0.72 / 0.71	0.61 / 0.61	0.61 / 0.60	0.54	0.54	0.66	0.48	0.55	0.56
N	2926	817	266	817	817	817	795	823	3117	795

575



576 In the Northern Hemisphere (Table 12), we find positive and comparably small biases for the two CBT products,
 577 NOAA-CDR and NT2-AMSR2, negative biases for all other products. We find the best quality of the linear agreement between
 578 PMW SIC and Landsat SIC for SICCI-25km, followed by SICCI-50km and SICCI-12km. According to Kern et al. (2020), the
 579 second half of May is characterized by an upswing of number and magnitude of SIC values > 100 % for SICCI-2 / OSI-450
 580 products (see Fig. S02 in the supplementary material). Using non-truncated SIC of these products reduces the mean bias by
 581 1.0 % for SICCI-12km, 0.5 % for SICCI-25km, and 0.3 % for OSI-450 and further improves the already good linear agreement.
 582 For SICCI-50km, results remain almost unchanged. We explain the difference in the response between SICCI-50km and
 583 SICCI-12km with the larger sensitivity of the higher frequency channels used by SICCI-12km to early stages of melt
 584 encountered at that time of the year.

585 Figure 9 illustrates a typical case of late summer melt conditions in the Ross Sea, Southern Ocean. The classified
 586 Landsat-8 image shows a heterogeneous mixture of black, grey and white pixels. The grey pixels denote a mixture of open
 587 water and thicker ice, possibly brash ice, sea ice with a wet or even flooded snow cover, or bare relatively thick ice from which
 588 the snow has been washed off. New/young ice is unlikely according to 6-hourly forecasts of the Antarctic Mesoscale Prediction
 589 System (AMPS) revealing near-surface temperatures around -1°C on January 27 2014 and between -3°C and -5°C on January
 590 28 and 29 2014 (<http://polarmet.osu.edu/AMPS/>, last access June 29, 2021), indicating that freeze-up has not yet commenced.
 591



592
 593 **Figure 9.** Landsat SIC, PMW SIC, and difference PMW SIC minus Landsat SIC for all ten products for a melt-condition case
 594 in the Ross Sea, Southern Ocean, on January 29, 2014. See Fig. 5 for more description of the maps shown.
 595



596 PMW SIC distributions match well with Landsat SIC, which is > 70 % for a considerable fraction of the map, but for
 597 most products PMW SIC is considerably smaller. Negative biases dominate and are widespread 30 % to 50 % in magnitude.
 598 Striking is the similarity between Landsat SIC 12.5km and ASI-SSMI, and between Landsat SIC 25 km and SICCI-25km as
 599 well as CBT-AMSR2. Striking is also the similarity between OSI-450, NT1-SSMI, CBT-SSMI and NOAA-CDR. These
 600 similarities indicate different native spatial resolutions, TB sampling intervals and grid spacings of, SSMI(S) on the one hand
 601 and AMSR-E(2) on the other hand, can cause a substantial difference in the agreement with independent SIC estimates such
 602 as from Landsat – especially when ice conditions are as heterogeneous as in this example (see Section 5.1). There is a notable
 603 fraction of positive biases, e.g. for ASI-SSMI – LSIC (see also Fig. S03 in the supplementary material) and NT2-AMSR –
 604 LSIC. NT2-AMSR – LSIC even tends to show more grid cells with positive than negative biases – not just in this case.

605 Overall, we find negative biases for nine of the ten products in the Southern Hemisphere (Table 13). These are smallest
 606 in magnitude for CBT-SSMI and NOAA-CDR: < 1 %, and largest for NT1-SSMI, ASI-SSMI and SICCI-50km. NT2-AMSR2
 607 stands out as the only product with a positive bias of 5 % (see Section 5.2). SICCI-25km and SICCI-50km again provide the
 608 best linear agreement with Landsat SIC (Table 13). Results for SICCI-2 products and OSI-450 improve when using non-
 609 truncated SIC (see also Fig. S01 in the supplementary material). In contrast to the Northern Hemisphere (see Table 12, Fig.
 610 S02 in the supplementary material), also SICCI-50km reveals a reduction of the bias and increase in the linear regression line
 611 slope. We attribute this to i) the presence of advanced melt conditions and ii) the different melt-induced snow and ice properties
 612 in the Southern Hemisphere comprising a larger fraction of coarse-grained snow due to pro-longed melt-freeze cycles and a
 613 generally drier snow surface, at least for the high-concentration parts of the sea-ice cover.

614 On the one hand, the negative biases (Figure 9, Table 13) agree well with results of earlier comparisons between
 615 Southern Hemisphere summer PMW SIC estimates and ship-based observations of the sea-ice cover (e.g. Worby and Comiso,
 616 2004; Ozsoy-Cicek et al., 2009). These studies hypothesize that under-estimation of the actual sea-ice concentration in PMW
 617 SIC products is primarily caused by wet, flooded sea ice exhibiting a similar surface emissivity as open water and hence
 618 looking like open water in PMW imagery. On the other hand, an unknown fraction of these negative biases could be caused
 619 by our Landsat SIC estimates being biased high because of the reasons laid out in Subsection 2.2.4 and the respective
 620 supplementary material.

621

622 **Table 13.** Summary of statistical results obtained for 45 melt-conditions cases in the Southern Hemisphere. See caption of
 623 Table 5 for an explanation of the parameters given. Numbers added behind the “/” for SICCI-2 products and OSI-450 denote
 624 results obtained using non-truncated SIC.

625

LS8, SH 2013-15	SICCI-12	SICCI-25	SICCI-50	OSI-450	CBT- SSMI	NOAA- CDR	CBT- AMSR2	NT1- SSMI	ASI- SSMI	NT2- AMSR2
Diff	-5.0 / -4.3	-5.8 / -5.5	-8.1 / -7.8	-4.9 / -4.6	-0.4	-0.6	-2.8	-8.7	-7.8	5.1
DiffSDEV	13.7 / 14.1	13.9 / 14.1	17.1 / 17.2	14.8 / 14.9	15.6	15.6	15.4	16.4	18.6	15.9
Slope	0.888/0.903	0.951/0.958	0.983/0.991	0.750/0.754	0.772	0.794	0.895	0.791	0.859	0.824
Intercept	4.0 / 3.5	-1.8 / -2.1	-6.7 / -7.1	14.1 / 15.4	18.0	16.0	5.8	8.2	3.6	19.4
R ²	0.79 / 0.78	0.78 / 0.78	0.69 / 0.69	0.71 / 0.71	0.69	0.69	0.72	0.67	0.65	0.69
N	10214	2915	916	2915	2899	2899	2955	2929	10129	2955

626



627 **5 Discussion**

628 **5.1 A note on grid resolutions**

629 SICCI-25km and SICCI-50km SIC have a grid resolution close to the actual algorithm resolution largely determined
630 by the native resolution of the lowest-frequency channel used (see field-of-view dimensions in Table 1). This is not the case
631 for, e.g. CBT-SSMI or OSI-450. Actually, we find a relatively poor performance of OSI-450 in comparison to SICCI-25km
632 (see Tables 5 to 7) – albeit the retrieval algorithm is exactly the same. We hypothesize that the coarser native resolution of the
633 satellite data used for OSI-450 provides one of the main explanations for this observation. SICCI-25km uses AMSR-E and
634 AMSR2 brightness temperatures observed at spatial resolutions (footprint sizes) between 14 km x 8 km (AMSR2: 12 km x 7
635 km) and 27 km x 16 km (AMSR2: 22 km x 14 km) (see Table 1). In contrast, OSI-450 uses SSM/I and SSMIS brightness
636 temperatures observed at footprint sizes between 37 km x 28 km and 69 km x 43 km. In addition, the relevant channels are
637 sampled spatially every 10 km for AMSR-E / AMSR2 and every 25 km for SSM/I / SSMIS. Therefore, spatial brightness
638 temperature variations caused, e.g., by variations in the open water fraction, can be identified at a finer spatial scale by AMSR-
639 E / AMSR2 than by SSM/I / SSMIS at the same frequency. The grid spacing at which OSI-450 and other SIC products relying
640 on SSMI(S) 19 / 37 GHz channels are provided is not the actual resolution of the estimated SIC. Surface information is smeared
641 in the SSMI(S) data much more. A similar observation applies to CBT-SSMI and CBT-AMSR. The latter provides SIC at a
642 grid resolution, which is closer to the algorithm resolution than that of CBT-SSMI; consequently, CBT-AMSR SIC agree
643 closer to Landsat SIC than CBT-SSMI SIC (see Tables 5, 6, and 7 and compare panels e) and g) in Fig. 2, 3 and 4). We are
644 confident that, besides the differences between the algorithms themselves, a substantial fraction of the observed difference in
645 the agreement with Landsat SIC is caused by the spatial representation of the true sea-ice concentration, which differs due to
646 the above-mentioned differences in satellite data used as input.

647 Our results confirm the stated impact of the native spatial resolution on potential biases between PMW SIC and
648 Landsat SIC very well. For instance, out of the ten products, ASI-SSMI and SICCI-12km both incorporating high-frequency,
649 fine spatial resolution imagery channels provide the 3rd and 4th best linear fits in the Northern Hemisphere (Tables 5, 6) and
650 the 3rd and 5th best linear fits in the Southern Hemisphere. When compared to the other SICCI-2 products, SICCI-12km has
651 considerably better results in the Southern than the Northern Hemisphere; SICCI-12km actually performs best out of the four
652 SICCI-2 / OSI-450 products (Table 7, Table S04 in the supplementary material). Our Landsat data set of the Southern
653 Hemisphere contains more cases of ice regimes (see Section 4) with variable open water fractions such as “heterogeneous ice”,
654 “leads / openings”, “freeze-up”, and “ice edge” than the one of the Northern Hemisphere (see Table S01 in the supplementary
655 material). Because a SIC product at finer spatial resolution is capable to depict such variable open water fractions better and
656 to observe the full SIC range more adequately it seems reasonable to have a better linear agreement between Landsat SIC and,
657 e.g., SICCI-12km SIC in the Southern than the Northern Hemisphere (compare Figs. 3 and 4 with respect to low SIC).

658 However, the other PMW SIC product with 12.5 km grid resolution, ASI-SSMI, does not show better results in the
659 Southern than the Northern Hemisphere when compared to, e.g. NT1-SSMI or SICCI-2 products. ASI-SSMI utilizes near-90
660 GHz brightness temperatures only while SICCI-12km combines near-90 GHz with 19 GHz brightness temperatures.
661 Atmospheric effects known to cause biases in near-90 GHz PMW SIC products (Kern, 2004; Ivanova et al., 2015) might
662 therefore have less impact on SICCI-12km than ASI-SSMI SIC. In addition, all SICCI-2 products utilize brightness
663 temperatures corrected for atmospheric effects using radiative transfer modelling while ASI-SSMI utilizes uncorrected
664 brightness temperatures. The fact that most of our Landsat scenes in the Southern Hemisphere represent atmospheric conditions
665 during summer melt and hence at a comparably higher water vapor load than in the Northern Hemisphere fits into this picture.
666 While the atmospheric effects are efficiently mitigated for SICCI-12km in both hemispheres these are larger for ASI-SSMI in
667 the Southern than the Northern Hemisphere.



668 **5.2 Hemispheric differences versus Landsat SIC bias**

669 At this point, we look at the difference between the SIC differences obtained in the Northern Hemisphere and the
670 Southern Hemisphere from a different perspective. Ice conditions represented by our Landsat SIC data set comprise more cases
671 with melt conditions and at the ice edge in the Southern Hemisphere (see Table S01 in the supplementary material). These
672 conditions are likely particularly subject to the positive bias in Landsat SIC due to mixed pixels described in Subsection 2.2.4
673 (see also the respective supplementary material). Therefore, we can expect that the positive SIC difference is, on average,
674 larger in the Southern than the Northern Hemisphere. We compare the differences listed in Tables 5, 6 and 7 and find the
675 following. OSI-450, SICCI-12km, and SICCI-25km exhibit small changes in the difference PMW SIC minus Landsat SIC
676 between +0.8 % and -0.8 %. NT2-AMSR reveals a positive change of +2.8 %. Both CBT products, NOAA-CDR, NT1-SSMI,
677 ASI-SSMI, and SICCI-50km show a negative change by between -2.2 % and -3.2 %. This change of ~ 3 % in the SIC difference
678 between the results of the Northern and the Southern Hemisphere is of the correct sign and of an order of magnitude we deem
679 a realistic estimate of the difference in the mentioned positive Landsat SIC bias between the hemispheres. What does this
680 mean? For example, for a PMW grid cell covered by an actual SIC of 95 %, due to the positive bias Landsat SIC might be 97
681 % in the Northern Hemisphere and 100 % in the Southern Hemisphere. A PMW SIC algorithm tuned equally well for the ice
682 conditions in the respective hemisphere would provide 95 % in both hemispheres. Compared to Landsat SIC this results in a
683 negative difference of -2 % in the Northern Hemisphere and of -5 % in the Southern Hemisphere, i.e. the difference becomes
684 even more negative. In contrast, the difference NT2-AMSR SIC minus Landsat SIC becomes even more positive, increasing
685 from +0.6 % in the Northern Hemisphere to +3.4 % in the Southern Hemisphere. When only considering the melt-condition
686 cases the overall difference increases from +1.7% to +5.1% (Tables 12, 13). Without further independent evaluation data to
687 better assess the accuracy of our Landsat SIC data we cannot draw a quantitative conclusion here. However, the increase in
688 the positive value of the difference PMW SIC minus Landsat SIC between the Northern and the Southern Hemisphere observed
689 for NT2-AMSR is opposite to our well-motivated suggestion that Landsat SIC values are biased higher in the Southern than
690 the Northern Hemisphere.

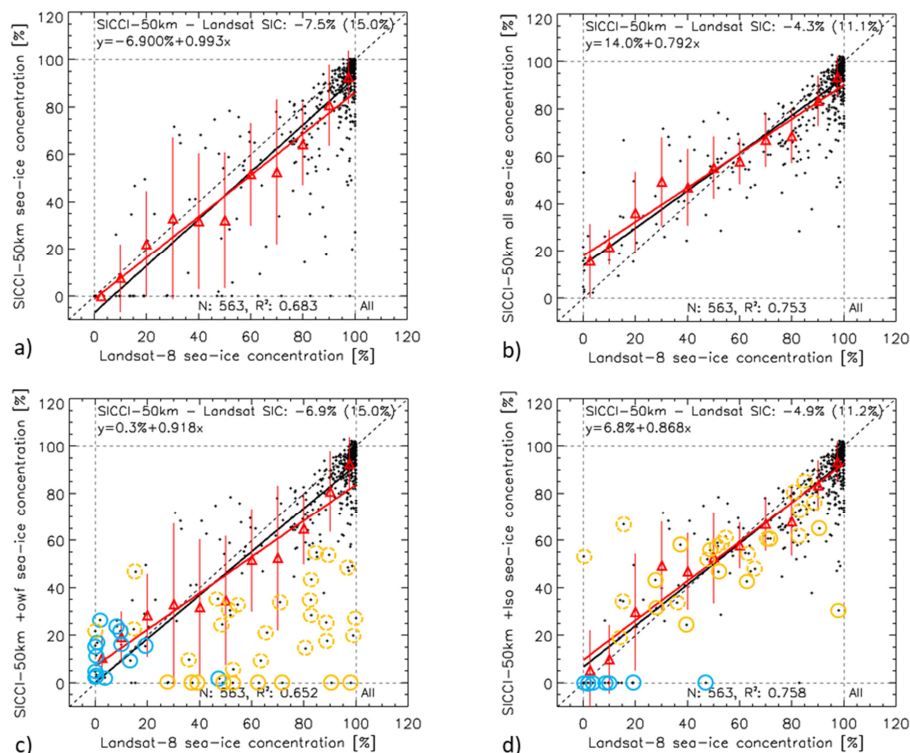
691 **5.3 A note on the effect of filters**

692 In this subsection, we comment on the observation that in the scatterplots of the Northern Hemisphere (Figs. 2 and 3)
693 particularly the SICCI-2 products but also OSI-450, CBT-AMSR and NT2-AMSR exhibit a relatively large number of cases
694 with PMW SIC = 0 % and Landsat SIC > 0 %. In addition, we find an unexpected high number of comparably low PMW SIC
695 values (< ~ 50 %) at Landsat SIC > ~ 70 %, especially for SICCI-50km (Fig. 2c, Fig. 3c). In the scatterplots of all products in
696 the Southern Hemisphere (Fig. 4) we observe a large number of cases with PMW SIC = 0 % and Landsat SIC > 0 %.

697 We hypothesize this observation is linked to the various filters applied. Examples of such filters are the weather or open
698 water filter (OWF) and the land spill-over filter (LSO). The OWF reduces the number of erroneous SIC values resulting from
699 unaccounted atmospheric influence, for example high cloud liquid water contents. OWF is effective along the ice edge and the
700 adjacent open water. One common realization of the OWF is to set PMW SIC values to 0 % SIC once brightness temperature
701 gradient ratios sensitive to the atmospheric influence exceed a certain threshold (e.g. Wensnahan et al., 1993; Spreen et al.,
702 2008; Lavergne et al., 2019). Such filters might cut off true SIC values (Andersen et al., 2006). The SICCI-2 and OSI-450
703 algorithm employs a modified version of such an OWF (Lavergne et al., 2019; Kern et al., 2019). The LSO reduces the number
704 of erroneous SIC values along coastlines resulting from unaccounted spillover of the (higher) land surface brightness
705 temperature into the (lower) open water brightness temperature. The LSO is particular effective during summer. It has also an
706 influence during the freezing season for situations where the coastline is only fringed by a quite narrow sea ice cover, as is the
707 case during fall freeze-up in the Hudson Bay or along the Siberian coast or during winter / spring along the coast of Greenland
708 facing the Irminger Sea. One realization of the LSO is a statistical approach, where the SIC of grid cells adjacent to the coast
709 is corrected, i.e. set to 0 % or interpolated to a more adequate value, based on SIC values within a certain neighborhood (e.g.



710 Cavalieri et al., 1999). The SICCI-2 and OSI-450 algorithm employs a novel attempt. Here the method of Maass and Kaleschke
 711 (2010) is used to correct for the land spillover already at the level of the brightness temperatures input to the SIC retrieval; the
 712 “classical” LSO filtering of Cavalieri et al. (1999) is still included, though (Lavergne et al., 2019). Note: the OWF sets PMW
 713 SIC to zero; the LSO reduces the PMW SIC to lower values but not necessarily to zero.
 714



715
 716 **Figure 10.** Scatterplots of SICCI-50km SIC (y-axis) versus Landsat SIC (x-axis) for ice regime “leads/openings” in the
 717 Southern Hemisphere in years 2013-2015. Black dots are individual data pairs, the black solid line is the linear regression, and
 718 the black dashed line is the identity line. Red triangles denote the mean PMW SIC computed for Landsat SIC ranges 0%-5%,
 719 5%-15%, 15%-25%, ..., 85%-95%, 95%-100%, the red bars one standard deviation of these mean values; the red line is the
 720 respective linear regression line. The overall difference PMW SIC minus Landsat SIC, its standard deviation, and the equation
 721 for the linear regression using the individual data pairs is given at the top, the number N of data pairs and the squared linear
 722 correlation coefficient at the bottom of each panel. Panel a) Fully truncated SIC, all filters applied; panel b) fully non-truncated
 723 SIC, no filters applied; panel c) truncated / non-truncated SIC, GT100 and OWF applied; panel d) truncated / non-truncated
 724 SIC, GT100 and LSO applied. Blue circles mark SICCI-50km SIC values set to 0 % by the OWF; orange circles mark SICCI-
 725 50km SIC values set changed by the LSO (solid circle: SIC set to 0 %, broken circle: SIC reduced).
 726

727 The SICCI-2 and OSI-450 products offer the full SIC distribution around 0 % and around 100 % SIC and the
 728 opportunity to reverse-engineer the effect of flags, i.e. switch the effect of certain flags on or off. Therefore, we are able to
 729 investigate the impact of the OWF and the LSO on our comparison results, an investigation not possible for the six other
 730 products. We choose the ice regime “leads/openings” in the Southern Hemisphere in years 2013-2015 and look, as an example
 731 for such an investigation, at the impact of the two above-mentioned filters on SICCI-50km SIC in comparison to Landsat SIC
 732 (Fig. 10). Note that we switch off these flags together with the near-100 % SIC flag to work with a more realistic SIC



733 distribution at the high-concentration end. The first finding is that there is not even one PMW SIC = 0 % in the fully non-
734 truncated, i.e. no filters applied, SIC scatterplot (Fig. 10b) – in contrast to the fully truncated SIC (Fig. 10a). Accordingly, the
735 statistical parameters differ considerably. For instance, the overall SIC difference reduces in magnitude from 7.5 % for the
736 fully truncated version of SICCI-50km to 4.3 % for fully non-truncated version; the standard deviation of the difference reduces
737 from 15.0 % to 11.1 %.

738 If we switch off the OWF, i.e. include the originally retrieved SIC values for those grid cells where the OWF is applied,
739 we get a number of SIC data pairs concentrated between Landsat SIC: 0 – 20 % and SICCI-50km: 0 – 30 % that can be clearly
740 associated with the OWF (compare Fig. 10 panel c) with panels a) and d). Statistical parameters change little. For instance, the
741 magnitude of the difference decreases by 0.5 % while the standard deviation stays the same. There is still a comparably large
742 number of cases with SICCI-50km SIC = 0 % or at least relatively low: < 30 %, concomitant with Landsat SIC > 50 %. If we
743 instead switch off the LSO, i.e. include the originally retrieved SIC values for those grid cells where the LSO is applied, we
744 find that almost all of the above-mentioned cases of low or equal-to-0 % SICCI-50km SIC can be traced back to substantially
745 higher SIC values (Fig. 10d). Statistical parameters change considerably. For instance, the magnitude of the difference changes
746 from 7.5 % (see above) to 4.9 % if keeping only the LSO filtered grid cells; the standard deviation of the difference reduces
747 from 15.0 % (see above) to 11.2 %. This reduction in the spread of values around the identity line is also evident very well in
748 the respective scatterplots (Fig. 10): the standard deviation of the Landsat SIC 10 % bin average SICCI-50km SIC (red vertical
749 bars) is much smaller in panel d) than panel a).

750 We observe a similar tendency for all other ice regimes where the LSO is applied, e.g. “freeze-up” or “melt conditions”,
751 in the Southern and in the Northern Hemisphere and for SICCI-25km and SICCI-12km as well (see Tables S04 and S05 in the
752 supplementary material). We note, however, that there are far fewer SIC data pairs subject to LSO filtering for OSI-450; hence
753 the effect of switching on or off the LSO is comparably small. We hypothesize that this could be explained with the different
754 native resolution of the satellite data used, the different sampling, and the different grid cell size and spacing. However, testing
755 this hypothesis is beyond the scope of this paper. For the SICCI-2 SIC products, we can confirm the hypothesis that the
756 comparably large number of PMW SIC = 0 % or < ~30 % across basically the entire SIC range (see Figs. 2, 3, and 4, panels
757 a) to c) can be explained with the application of an LSO resulting in an elevated number of cases with PMW SIC smaller than
758 Landsat SIC. This provides a viable explanation for unexpectedly large SIC differences observed for SICCI-50km along
759 coastlines, of particularly Greenland or the Eastern Antarctic, reported in Kern et al. (2019, their Fig. 8 c) and Fig. 11 c).
760 Whether this is due to the land spillover correction at the brightness temperature level (Maass and Kaleschke, 2010) or the
761 statistical filtering (Cavalieri et al., 1999) remains to be investigated. We clearly see it as an advantage that for SICCI-2 and
762 OSI-450 products we can switch off filters and in a reverse-engineering way investigate the impact these filters have on PMW
763 SIC. This appears not to be possible for the remaining six PMW SIC products. Application of the LSO can produce an
764 artificially large number of SIC values near or at 0 % that agree less well with the Landsat SIC than the originally retrieved
765 SIC values – as we demonstrate for the SICCI-2 and OSI-450 products. As a consequence, results of an evaluation including
766 a considerable number of near-coastal grid cells need to be interpreted carefully. The number of artificially low SIC values
767 resulting from the LSO for the other six PMW SIC products is unknown as is their impact on the evaluation results shown in
768 this paper.

769 6 Summary and Conclusions

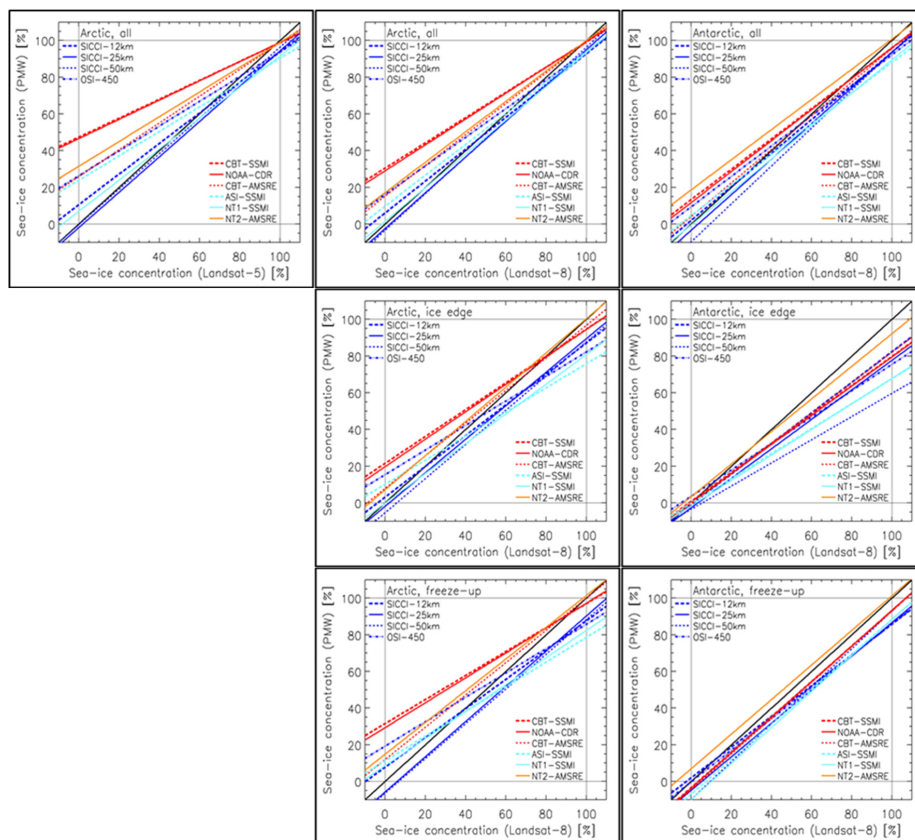
770 In this paper, we present results of an evaluation of ten passive microwave (PMW) SIC products against SIC estimates
771 derived from a total of more than 300 clear-sky Landsat visible images acquired in the Northern Hemisphere during mostly
772 late winter / spring (March through May) and in the Southern Hemisphere during spring / summer / early fall (October through
773 March). We estimate Landsat SIC at the grid resolution of the PMW SIC products using results of supervised classification of



774 Landsat broadband albedo maps into ice and water at 30 m pixel resolution. The comparison between PMW and Landsat SIC
775 is carried out based on all valid collocated SIC map pairs but also based on subsets of these pairs defining certain ice regimes.
776 These ice regimes are “high concentration”, “freeze-up”, “ice edge”, “leads/openings”, “heterogeneous ice”, and “melt
777 conditions”.

778 Our comparison uses parameters such as the mean difference between PMW and Landsat SIC and its standard deviation,
779 the median difference, and parameters describing the linear agreement: slope and intercept of a linear regression and the linear
780 regression coefficient. We summarize these parameters in Figures 11 and 12 and come up with the following conclusions.

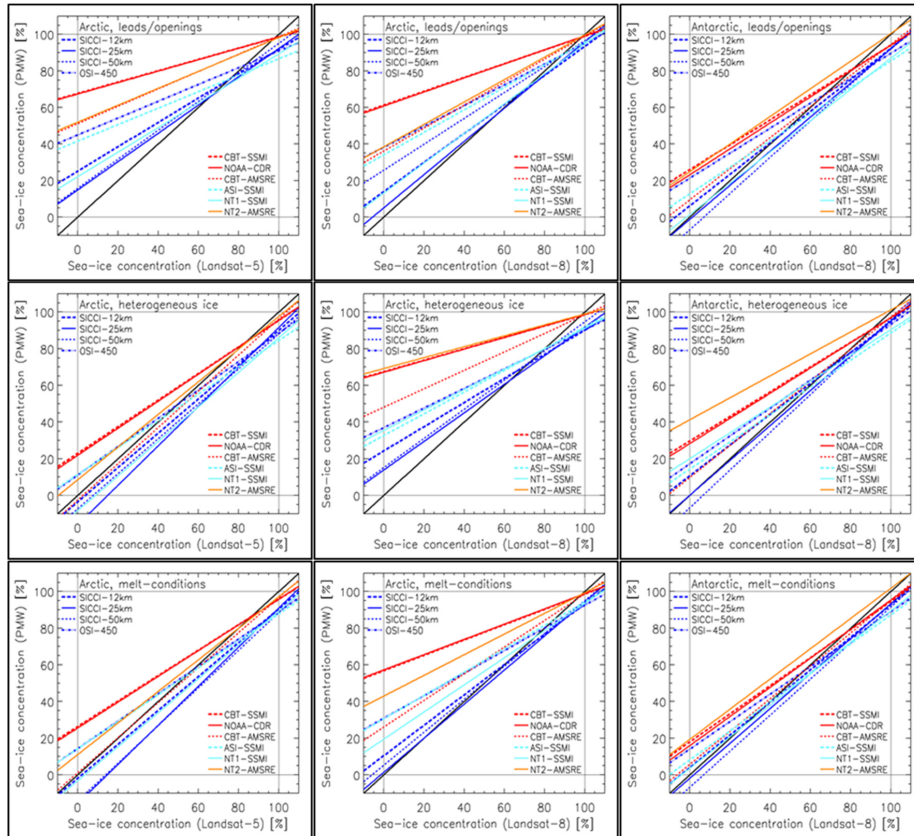
781



782

783 **Figure 11.** Summary of all linear regression lines obtained for the comparison between Landsat SIC and PMW SIC for all ice
784 regimes – except high-concentration ice. Columns denote, from left to right, Landsat-5 Arctic (i.e. first-year ice), Landsat-8
785 Arctic (i.e. mixed first-year / multiyear ice and multiyear ice), and Landsat-8 Antarctic. Ice regimes are sorted per row from
786 top to bottom: “all” cases, “ice edge”, and “freeze-up”. Different colors and line styles denote different products as indicated.
787 The black solid line denotes the identity line.

788



789

790 **Figure 11.** continued for ice regimes “leads and coastal openings”, “heterogeneous ice”, “melt-conditions”.

791

792 • It is important to take an integrated view of these parameters because, for instance, a small overall bias is not necessarily
 793 associated with a good linear agreement across the entire SIC range and a perfect linear agreement with a slope close to
 794 unity and a high correlation could be associated with a large overall bias.

795 • It is also important to take into account the expected influences of, e.g. melt conditions (section 4.3), fraction of new/thin
 796 ice (section 4.1) as well as sub-pixel size ocean-ice mixture (Section 2.2.4) on both PMW SIC and Landsat SIC.

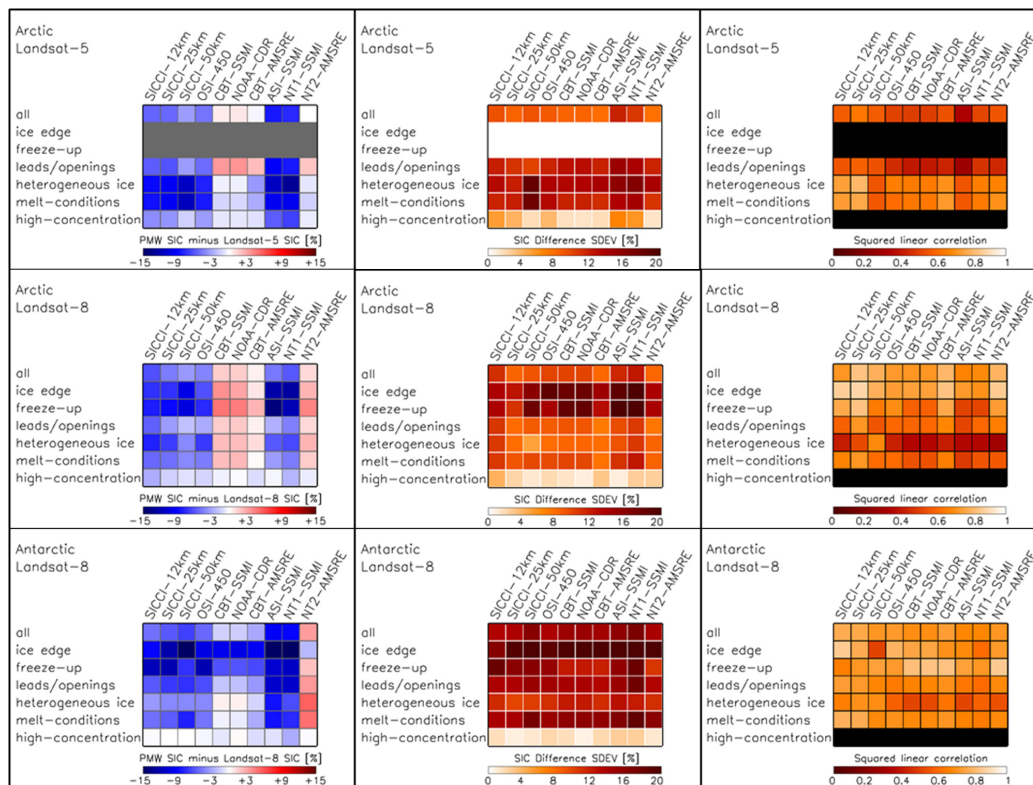
797 • SICCI-25km and SICCI-50km SIC offer overall the best linear agreement to Landsat SIC as demonstrated in Fig. 11 and
 798 Fig. 12, right column. This is illustrated as well by mean and median PMW SIC values computed for Landsat SIC bins
 799 aligned very well along the identity line (Figs. 2 to 4), with exceptions being explainable by filters applied in the products
 800 (see Section 5.3). The magnitude of the difference PMW SIC minus Landsat SIC is, however, larger than for the two
 801 CBT-products and NOAA-CDR, almost without exception (Fig. 12, left column).

802 • The two CBT products, NOAA-CDR and NT2-AMSR offer the smallest overall magnitude of the difference PMW SIC
 803 minus Landsat SIC (Fig. 12, left column). Except for CBT-AMSR2 in the Southern Hemisphere, mean and median PMW
 804 SIC values align less well along the identity line than for SICCI-25km and SICCI-50km in Figs 2 to 4. The linear
 805 agreement is considerably worse than for SICCI-25km and SICCI-50km (Fig. 11, Fig. 12, right column).

806 • NT2-AMSR is the only product over-estimating Landsat SIC in the Southern Hemisphere – overall but also for almost all
 807 ice regimes. This is problematic in view of the potential positive bias of Landsat SIC for ice conditions with an elevated
 808 number of mixed ocean-ice Landsat pixels (see Subsection 2.2.4), e.g. ice regimes “melt conditions”, “ice edge” and
 809 “freeze-up”.



810



811

812 **Figure 12.** Illustration of the statistical parameters of the comparison between Landsat SIC and PMW SIC for all ice regimes.
 813 Rows denote, from top to bottom, first-year ice Arctic (Landsat-5), mixed first-year / multiyear ice and multiyear ice Arctic
 814 (Landsat-8), and all ice Antarctic (Landsat-8). Columns denote, from left to right, accuracy (difference PMW SIC minus
 815 Landsat SIC), precision (standard deviation of the SIC difference), and squared linear correlation coefficient. The uni-colored
 816 rows denote cases left out, either because these ice regimes are not populated (topmost row of panels) or because the retrieval
 817 of parameters did not make sense (Squared linear correlation for ice regime “high concentration”).

818

819 All products provide SIC data truncated to the range 0 % to 100 % albeit all algorithms but NT2-AMSRE use a SIC
 820 retrieval procedure which in principle provides a full SIC distribution around the end-members 0 % and 100 %. Only the
 821 SICCI-2 products and OSI-450 allow consideration of the full SIC distribution. While our main results are derived with the
 822 truncated SIC distribution, we demonstrate that, without exception, using the full SIC distribution reduces the mean difference
 823 and enhances the quality of the linear agreement between PMW SIC and Landsat SIC which is already superior for SICCI-
 824 25km and SICCI-50km. It is important to consider when comparing the results obtained with the ten products against each
 825 other in order to avoid misinterpretation. While we obtain smallest SIC differences for the two CBT products, NOAA-CDR
 826 and NT2-AMSRE/2, this is likely to change using the full SIC distribution. This applies in particular to ice regimes “high-
 827 concentration” (section 4.2) and “melt conditions”, but also to the full set of SIC data pairs (denoted “all” in Fig. 12). The
 828 impact this difference in the comprehensiveness of the SIC products has on our evaluation results prevents us from making a
 829 ranking between the SIC products.

830

831 This paper is limited to clear-sky visible imagery. It is hence impossible to evaluate the performance of the SIC products
 832 under the full set of possible weather conditions with an influence on the SIC retrieval, i.e. surface wind speed and atmospheric
 water vapor and cloud liquid water content. We note that our results likely cover a certain range of surface wind speeds and



833 atmospheric water vapor contents which we, however, did not quantify, e.g. by means of atmospheric reanalysis data, to stay
834 focused. Obviously, this would be an issue worth pursuing in a forthcoming study for which SIC estimates based on SAR data
835 have to be used. These might allow to assess PMW SIC quality also under higher loads of atmospheric water vapor content
836 and, more importantly, clouds. Such a study could then focus in particular on an improved accuracy assessment of the PMW
837 SIC in the marginal ice zone and along the ice edge. In such regions, our approach to derive Landsat SIC likely results in the
838 highest positive biases – between a few to in the worst case 20 % for single PMW grid cells – due to mixed ocean-ice Landsat
839 pixels classified as ice. Such a study would also be an excellent opportunity to evaluate the weather filters currently employed
840 in the SIC products. In order to have a meaningful sample, such a study would require an equally large number of SAR images
841 interpreted into well-evaluated SIC estimates for a number of years covering both hemispheres as is used in this paper. This
842 calls for continued development of reliable and consistent SIC estimates from SAR and, thorough evaluation of SAR SIC
843 products in both hemispheres.

844 *Data availability.* All sea-ice concentration products except SICCI-12km are publicly available from the sources provided in
845 the reference list or in Kern et al. (2019). The SICCI-12km product is available upon request from T. Lavergne. The
846 classified Landsat images are available from <https://doi.org/10.25592/uhhfdm.9181> (last access: July 9 2021).

847 *Author contributions.* SK wrote the manuscript. TL, LTP and RT contributed to the concept and work presented in the paper
848 and also assisted in the writing. SK performed the data analysis together with LB, MM, and LZ. SK conducted the inter-
849 comparison with contributions in the interpretation of the results from TL, LTP and RT.

850 *Competing interests.* The authors declare that they have no conflict of interest.

851
852 *Acknowledgements.* The work presented here was funded by EUMETSAT (through the 3rd Continuous Developments and
853 Operation Phase of OSI SAF) and ESA (through the Climate Change Initiative Sea_Ice_cci project), and the German Research
854 Foundation (DFG) Excellence Initiative CLISAP under Grant EXC 177/2. The publication contributes to the Cluster of
855 Excellence ‘CLICCS – Climate, Climatic Change, and Society’ and to the Center for Earth System Research and Sustainability
856 (CEN) of the University of Hamburg.

857 7 References

- 858 Andersen, S., Tonboe, R. T., Kern, S., and Schyberg, H.: Improved retrieval of sea ice total concentration from spaceborne
859 passive microwave observations using Numerical Weather Prediction model fields: An intercomparison of nine algorithms.
860 *Rem. Sens. Environ.*, 104(4), 374-392, 2006.
- 861 Andersen, S., Pedersen, L. T., Heygster, G., Tonboe, R. T., and Kaleschke, L.: Intercomparison of passive microwave sea ice
862 concentration retrievals over the high concentration Arctic sea ice. *J. Geophys. Res.*, 112, C08004,
863 <https://doi.org/10.1029/2006JC003543>, 2007.
- 864 Barsi, J. A., Kenton, L., Kvaran, G., Markham, B. L., and Pedelty, J. A.: The spectral response of the Landsat-8 operational
865 land imager. *Rem. Sens.*, 6(10), 10232-10251, <https://doi.org/10.3390/rs61010232>, 2014.
- 866 Belchansky, G. I., and Douglas, D. C.: Seasonal comparisons of sea ice concentration estimates derived from SSM/I, OKEAN,
867 and RADARSAT data. *Rem. Sens. Environ.*, 81, 67-81, 2002.
- 868 Boutin, G., Lique, C., Arduin, F., Rousset, C., Talandier, C., Accensi, M., and Girard-Arduin, F.: Towards a coupled model
869 to investigate wave-sea ice interactions in the Arctic marginal ice zone. *The Cryosphere*, 14(2), 709-735,
870 <https://doi.org/10.5194/tc-14-709-2020>, 2020.
- 871 Brandt, R. E., Warren, S. G., Worby, A. P., and Grenfell, T. C.: Surface Albedo of the Antarctic sea ice zone. *J. Climate*, 18,
872 3606-3622, 2005.
- 873 Burgard, C., Notz, D., Pedersen, L. T., and Tonboe, R. T.: The Arctic Ocean Observation Operator for 6.9 GHz (ARC3O) –
874 Part 1: How to obtain sea ice brightness temperatures at 6.9 GHz from climate model output. *The Cryosphere*, 14(7), 2369–
875 2386, <https://doi.org/10.5194/tc-14-2369-2020>, 2020.



- 876 Cavalieri, D. J.: A microwave technique for mapping thin sea ice. *J. Geophys. Res.*, 99(C6), 12561-12572, 1994.
- 877 Cavalieri D. J., Gloersen, P., and Campbell, W. J.: Determination of Sea Ice Parameters with the NIMBUS 7 SMMR. *J.*
- 878 *Geophys. Res.*, 89(D4), 5355-5369, 1984.
- 879 Cavalieri, D. J., Crawford, M., Drinkwater, W. J., Emery, D. T., Eppler, L. D., Farmer, M., Goodberlet, R., Jentz, A., Milman,
- 880 C. Morris, R. Onstott, A. Schweiger, R. Shuchman, K. Steffen, C. T. Swift, C. Wackerman, and R. L. Weaver. 1992. NASA
- 881 sea ice validation program for the DMSP SSM/I: final report. NASA Technical Memorandum 104559. National Aeronautics
- 882 and Space Administration, Washington, D.C. 126 pages.
- 883 Cavalieri, D. J., Parkinson, C. L., Gloersen, P., Comiso, J. C., and Zwally, H. J.: Deriving long-term time series of sea ice
- 884 cover from satellite passive-microwave multisensor data sets. *J. Geophys. Res.*, 104(C7), 15803–15814,
- 885 <http://doi.org/10.1029/1999JC900081>, 1999.
- 886 Cavalieri, D. J., Markus, T., Hall, D. K., Gasiewski, A. J., Klein, M., and Ivanoff, A.: Assessment of EOS Aqua AMSR-E
- 887 Arctic sea ice concentrations using Landsat-7 and airborne microwave imagery. *IEEE Trans. Geosci. Rem. Sens.*, 44(11),
- 888 3057-3069, <https://doi.org/10.1109/TGRS.2006.878445>, 2006.
- 889 Chander, G., Markham, B. L., and Barsi, J. A.: Revised Landsat-5 Thematic Mapper Radiometric Calibration. *IEEE Geosci.*
- 890 *Rem. Sens. Lett.*, 4(3), 490-494, 2007.
- 891 Chander, G., Markham, B. L., and Helder, D. L.: Summary of current radiometric calibration coefficients for Landsat MSS,
- 892 TM, ETM+, and EO-1 ALI sensors. *Rem. Sens. Environ.*, 113, 893-903, 2009.
- 893 Cheng, A., Casati, B., Tivy, A., Zagon, T., Lemieux, J.-F., and Tremblay, L. B.: Accuracy and inter-analyst agreement of
- 894 visually estimated sea ice concentrations in Canadian Ice Service ice charts using single-polarization RADARSAT-2. *The*
- 895 *Cryosphere*, 14(4), 1289-1310, <https://doi.org/10.5194/tc-14-1289-2020>, 2020.
- 896 Comiso J. C.: Characteristics of arctic winter sea ice from satellite multispectral microwave observations. *J. Geophys. Res.*,
- 897 91(C1), 975-994, 1986.
- 898 Comiso, J. C.: Enhanced sea ice concentrations and ice extents from AMSR-E data. *J. Rem. Sens. Soc. Japan*, 29(1), 199-215,
- 899 2009.
- 900 Comiso, J. C., and Zwally, H. J.: Antarctic sea ice concentrations inferred from Nimbus 5 ESMR and Landsat imagery. *J.*
- 901 *Geophys. Res.*, 87(C8), 5836-5844, <https://doi.org/10.1029/JC087iC08p05836>, 1982.
- 902 Comiso, J. C., and Steffen, K.: Studies of Antarctic sea ice concentrations from satellite data and their applications. *J. Geophys.*
- 903 *Res.*, 106(C12), 31,361-31,385, 2001.
- 904 Comiso, J. C., and Nishio, F.: Trends in the sea ice cover using enhanced and compatible AMSR-E, SSM/I, and SMMR data. *J.*
- 905 *Geophys. Res.*, 113, C02S07, <http://doi.org/10.1029/2007JC004257>, 2008.
- 906 Comiso, J. C., Wadhams, P., Krabill, W. B., Swift, R. N., Crawford, J. P., and Tucker III, W. B.: Top/bottom multisensory
- 907 remote sensing of Arctic sea ice. *J. Geophys. Res.*, 96(C2), 2693-2709, <https://doi.org/10.1029/90JC02466>, 1991.
- 908 Comiso, J. C., Cavalieri, D. J., Parkinson, C. L., and Gloersen, P.: Passive microwave algorithms for sea ice concentration: A
- 909 comparison of two techniques. *Rem. Sens. Environ.*, 60(3), 357-384, 1997.
- 910 Comiso, J. C., Cavalieri, D. J., and Markus, T.: Sea ice concentration, ice temperature, and snow depth, using AMSR-E data.
- 911 *IEEE Trans. Geosci. Rem. Sens.*, 41(2), 243-252, <https://doi.org/10.1109/TGRS.2002.808317>, 2003.
- 912 Cooke, C. L. V., and Scott, K. A.: Estimating sea ice concentration from SAR: Training convolutional neural networks with
- 913 passive microwave data. *IEEE Trans. Geosci. Rem. Sens.*, 57(7), 4735-4747, <https://doi.org/10.1109/TGRS.2019.2892723>,
- 914 2019.
- 915 Dokken, S. T., Håkansson, B., and Askne, J.: Inter-comparison of Arctic sea ice concentration using RADARSAT, ERS, SSM/I
- 916 and In-Situ Data. *Can. J. Rem. Sens.*, 26(6), 521-536, <https://doi.org/10.1080/07038992.2000.10874793>, 2000.



- 917 Drusch, M., Del Bello, U., Carlier, S., Colin, O., Fernandez, V., Gascon, F., Hoersch, B., Isola, C., Laberinti, P., Martimort,
918 P., Meygret, A., Spoto, F., Sy, O., Marchese, F., and Bargellini, P.: Sentinel-2: ESA's optical high-resolution mission for
919 GMES operational services. *Rem. Sens. Environ.*, 120, 25-36, <https://doi.org/10.1016/j.res.2011.11.026>, 2012.
- 920 Ezraty, R., Girard-Arduin, F., Piollé, J.-F., Kaleschke, L., and Heygster, G.: Arctic and Antarctic sea ice concentration and
921 Arctic sea ice drift estimated from special sensor microwave data – Users's Manual, Version 2.1, IFREMER, Brest, France,
922 February 2007.
- 923 Han, H., and Kim, H.-C.: Evaluation of summer passive microwave sea ice concentrations in the Chukchi Sea based on
924 KOMPSAT-5 SAR and numerical weather prediction data. *Rem. Sens. Environ.*, 209, 343-362,
925 <https://doi.org/10.1016/j.rse.2018.02.058>, 2018.
- 926 Heinrichs, J. F., Cavalieri, D. J., and Markus, T.: Assessment of the AMSR-E sea ice concentration product at the ice edge
927 using RADARSAT-1 and MODIS imagery. *IEEE Trans. Geosci. Rem. Sens.*, 44(11), 3070-3080,
928 <https://doi.org/10.1109/TGRS.2006.880622>, 2006.
- 929 Ivanova, N., Johannessen, O. M., Pedersen, R. T., and Tonboe, R. T.: Retrieval of Arctic sea ice parameters by satellite passive
930 microwave sensors: A comparison of eleven sea ice concentration algorithms. *IEEE Trans. Geosci. Rem. Sens.*, 52(11), 7233-
931 7246, <http://doi.org/10.1109/TGRS.2014.2310136>, 2014.
- 932 Ivanova, N., Pedersen, L. T., Tonboe, R. T., Kern, S., Heygster, G., Lavergne, T., Sørensen, A., Saldo, R., Dybkjær, G.,
933 Brucker, L., and Shokr, M.: Inter-comparison and evaluation of sea ice algorithms: towards further identification of challenges
934 and optimal approach using passive microwave observations. *The Cryosphere*, 9(5), 1797-1817, <http://doi.org/10.5194/tc-9-1797-2015>, 2015.
- 935
- 936 Kaleschke, L., Lüpkes, C., Vihma, T., Haarpaintner, J., Bochert, A., Hartmann, J., and Heygster, G.: SSM/I sea ice remote
937 sensing for mesoscale ocean-atmosphere interaction analysis. *Can. J. Rem. Sens.*, 27(5), 526-537, 2001.
- 938 Karvonen, J.: A sea ice concentration estimation algorithm utilizing radiometer and SAR data. *The Cryosphere*, 8(5), 1639-
939 1650, <https://doi.org/10.5194/tc-8-1639-2014>, 2014.
- 940 Karvonen, J.: Baltic sea ice concentration estimation using SENTINEL-1 SAR and AMSR2 microwave radiometer data. *IEEE*
941 *Trans. Geosci. Rem. Sens.*, 55(5), 2871-2883, <https://doi.org/10.1109/TGRS.2017.2655567>, 2017.
- 942 Kern, S.: A new method for medium-resolution sea ice analysis using weather-influence corrected Special Sensor
943 Microwave/Imager 85 GHz data. *Int. J. Rem. Sens.*, 25(21), 4555-4582, 2004.
- 944 Kern, S., Kaleschke, L., and Clausi, D. A.: A comparison of two 85-GHz SSM/I ice concentration algorithms with AVHRR
945 and ERS-2 SAR imagery. *IEEE Trans. Geosci. Rem. Sens.*, 41(10), 2294-2306, <https://doi.org/10.1109/TGRS.2003.817181>,
946 2003.
- 947 Kern, S., Lavergne, T., Notz, D., Pedersen, L., Tonboe, R., Saldo, R., and Sørensen, A. M.: Satellite passive microwave sea-
948 ice concentration data set intercomparison: closed ice and ship-based observations. *The Cryosphere*, 13(12), 3261-3307,
949 <http://doi.org/10.5194/tc-13-3261-2019>, 2019.
- 950 Kern, S., Lavergne, T., Notz, D., Pedersen, L. T., and Tonboe, R.: Satellite passive microwave sea-ice concentration data set
951 intercomparison for Arctic summer conditions. *The Cryosphere*, 14(7), 2469-2493, <https://doi.org/10.5194/tc-14-2469-2020>,
952 2020.
- 953 Knap, W. H., Brock, B. W., Oerlemans, J., and Willis, I. C.: Comparison of Landsat TM-derived and ground-based albedos of
954 Haut Glacier d'Arolla, Switzerland. *Int. J. Rem. Sens.*, 20(17), 3293-3310, 1999.
- 955 Koepke, P.: Removal of Atmospheric Effects from AVHRR albedos. *J. Appl. Meteorol.*, 28, 1341-1348, 1989.
- 956 Komarov, A. S., and Buehner, M.: Automated detection of ice and open water from dual-polarization RADARSAT-2 images
957 for data assimilation. *IEEE Trans. Geosci. Rem. Sens.*, 55(10), 5755-5769, <https://doi.org/10.1109/TGRS.2017.2713987>,
958 2017.



- 959 Komarov, A. S., and Buehner, M.: Improved retrieval of ice and open water from sequential RADARSAT-2 images. *IEEE*
960 *Trans. Geosci. Rem. Sens.*, 57(6), 3694-3702, <https://doi.org/10.1109/TGRS.2018.2886685>, 2019.
- 961 Kwok, R.: Sea ice concentration estimates from satellite passive microwave radiometry and openings from SAR ice motion.
962 *Geophys. Res. Lett.*, 29(9), 1311, <https://doi.org/10.1029/2002GL014787>, 2002.
- 963 Lavergne, T., Macdonald Sørensen, A., Kern, S., Tonboe, R., Notz, D., Aaboe, S., Bell, L., Dybkjær, Eastwood, S., Gabarro,
964 C., Heygster, G., Killie, M., Brandt Kreiner, M., Lavelle, J., Saldo, R., Sandven, S., and Pedersen, L.: Version 2 of the
965 EUMETSAT OSI SAF and ESA-CCI sea-ice concentration climate data records. *The Cryosphere*, 13(1), 49–78,
966 <http://doi.org/10.5194/tc-13-49-2019>, 2019.
- 967 Leigh, S., Wang, Z., and Clausi, D. A.: Automated ice-water classification using dual polarization SAR satellite imagery. *IEEE*
968 *Trans. Geosci. Rem. Sens.*, 52(9), 5529-5539, <https://doi.org/10.1109/TGRS.2013.2290231>, 2014.
- 969 Liu, Y., Key, J., and Mahoney, R.: Sea and freshwater ice concentration from VIIRS on Suomi NPP and the future JPSS
970 satellites. *Rem. Sens.*, 8(6), 523-542, <https://doi.org/10.3390/rs8060523>, 2016.
- 971 Lohse, J., Douglgeris, A. P., and Dierking, W.: An optimal decision-tree design strategy and its application to sea ice
972 classification from SAR imagery. *Rem. Sens.*, 11(13), 1574-1588, <https://doi.org/10.3390/rs11131574>, 2019.
- 973 Lu, J., Heygster, G., and Spreen, G.: Atmospheric correction of sea-ice concentration retrieval for 89GHz AMSR-E
974 observations. *IEEE J. Sel. Topics Appl. Earth. Obs. Rem. Sens.*, 11(5), 1442-1457,
975 <https://doi.org/10.1109/JSTARS.2018.2805193>, 2018.
- 976 Lu, P., Li, Z. L., Zhang, Z. H., and Dong, X. L.: Aerial observations of floe size distributions in the marginal ice zone of
977 summer Prydz Bay. *J. Geophys. Res.*, 113, C02011, <https://doi.org/10.1029/2006JC003965>, 2008.
- 978 Maass, N., and Kaleschke, L.: Improving passive microwave sea ice concentration algorithms for coastal areas: applications
979 to the Baltic Sea. *Tellus*, 62A(4), 393-410, <https://doi.org/10.1111/j.1600-0870.2010.00452.x>, 2010.
- 980 Malmgren-Hansen, D., Pedersen, L. T., Aasbjerg Nielsen, A., Brandt Kreiner, M., Saldo, R., Skriver, H., Lavelle, J., Buus-
981 Hinkler, J., and Harnvig Krane, K.: A convolutional neural network architecture for sentinel-1 and AMSR2 data fusion. *IEEE*
982 *Trans. Geosci. Rem. Sens.*, 59(3), 1890-1902, <https://doi.org/10.1109/TGRS.2020.3004539>, 2020.
- 983 Marcq, S., and Weiss, J.: Influence of sea ice lead-width distribution on turbulent heat transfer between the ocean and the
984 atmosphere. *The Cryosphere*, 6(1), 143-156, <https://doi.org/10.5194/tc-6-143-2012>, 2012.
- 985 Markus, T., and Cavalieri, D. J.: An enhancement of the NASA Team sea ice algorithm. *IEEE Trans. Geosci. Rem. Sens.*,
986 38(3), 1387-1398, 2000.
- 987 Markus, T., and Cavalieri, D. J.: The AMSR-E NT2 sea ice concentration algorithm: its basis and implementation. *J. Rem.*
988 *Sens. Soc. Japan*, 29(1), 216-225, 2009.
- 989 Markus, T., and Dokken, S. T.: Evaluation of late summer passive microwave Arctic sea ice retrievals. *IEEE Trans. Geosci.*
990 *Rem. Sens.*, 40(2), 348-356, 2002.
- 991 Meier, W. N.: Comparison of passive microwave ice concentration algorithm retrievals with AVHRR imagery in Arctic
992 peripheral seas. *IEEE Trans. Geosci. Rem. Sens.*, 43(6), 1324-1337, <http://doi.org/10.1109/TGRS.2005.846151>, 2005.
- 993 Meier, W. N., and Windnagel, A.: Sea ice concentration – climate algorithm theoretical basis document, NOAA Climate Data
994 Record Program CDRP-ATBD-0107 Rev. 7 (03/06/2018), available at [https://www.ncdc.noaa.gov/cdr/oceanic/sea-ice-](https://www.ncdc.noaa.gov/cdr/oceanic/sea-ice-concentration)
995 [concentration](https://www.ncdc.noaa.gov/cdr/oceanic/sea-ice-concentration), 2018.
- 996 Meier, W. N., T. Markus, and J. C. Comiso, AMSR-E/AMSR2 Unified L3 Daily 25.0 km Brightness Temperatures, Sea Ice
997 Concentration, Motion & Snow Depth Polar Grids, Version 1, Boulder, Colorado USA, NASA National Snow and Ice Data
998 Center Distributed Active Archive Center, 2018, <https://doi.org/10.5067/TRUIAL3WPAUP>, [last access: July 13, 2021], 2018.
- 999 Meier, W. N., Fetterer, F., Savoie, M., Mallory, S., Duerr, R., and Stroeve, J.: *NOAA/NSIDC Climate Data Record of Passive*
1000 *Microwave Sea Ice Concentration, Version 3*. Boulder, Colorado USA. NSIDC: National Snow and Ice Data Center.
1001 <http://doi.org/10.7265/N59P2ZTG>, [last access: July 13, 2021], 2017.



- 1002 Mojica Moncada, J. F., and Holland, D.: Automatic Weather Station Pine Island Glacier, U.S. Antarctic Program (USAP) Data
1003 Center. <https://doi.org/10.15784/601216> [last access: June 29, 2021], 2019.
- 1004 Nose, T., Waseda, T., Kodaira, T., and Inoue, J.: Satellite-retrieved sea ice concentration uncertainty and its effect on modelling
1005 wave evolution in marginal ice zones. *The Cryosphere*, 14(6), 2029-2052, <https://doi.org/10.5194/tc-14-2029-2020>, 2020.
- 1006 Ochilov, S., and Clausi, D. A.: Operational SAR sea-ice image classification. *IEEE Trans. Geosci. Rem. Sens.*, 50(11), 4397-
1007 4408, <https://doi.org/10.1109/TGRS.2012.2192278>, 2012.
- 1008 Onana, V.-De-P., Kurtz, N. T., Farrell, S. L., Koenig, L. S., Studinger, M., and Harbeck, J. P.: A sea-ice lead detection
1009 algorithm for use with high-resolution airborne visible imagery. *IEEE Trans. Geosci. Rem. Sens.*, 51(1), 38-56,
1010 <https://doi.org/10.1109/TGRS.2012.2202666>, 2013.
- 1011 Ozsoy-Cicek, B., Xie, H., Ackley, S. F., and Ye, K.: Antarctic summer sea ice concentration and extent: comparison of ODEN
1012 2006 ship observations, satellite passive microwave and NIC sea ice charts. *The Cryosphere*, 3, 1-9, <https://doi.org/10.5194/tc-3-1-2009>, 2009.
- 1014 Paget, M. J., Worby, A. P., and Michael, K. J.: Determining the floe-size distribution of East Antarctic sea ice from digital
1015 aerial photographs. *Ann. Glaciol.*, 33, 94-100, 2001.
- 1016 Pegau, W. S., and Paulson, C. A.: The albedo of Arctic leads in summer. *Ann. Glaciol.*, 33, 221-224, 2001.
- 1017 Peng, G., and Meier, W. N.: Temporal and regional variability of Arctic sea-ice coverage from satellite data. *Ann. Glaciol.*,
1018 59(76, part 2), 191-200, <http://doi.org/10.1017/aog.2017.32>, 2018.
- 1019 Peng, G., Meier, W. N., Scott, D., and Savoie, M.: A long-term and reproducible passive microwave sea ice concentration data
1020 record for climate studies and monitoring. *Earth Syst. Sci. Data*, 5, 311-318. <http://doi.org/10.5194/essd-5-311-2013>, 2013.
- 1021 Perovich, D. K., and Jones, K. F.: The seasonal evolution of sea ice floe size distribution. *J. Geophys. Res.-Oceans*, 119, 8767-
1022 8777, <https://doi.org/10.1002/2014JC010136>, 2014.
- 1023 Singha, S., Johansson, M., Hughes, N., Hvidegaard, S. M., and Skourup, H.: Arctic sea ice characterization using spaceborne
1024 fully polarimetric L-, C-, and X-band SAR with validation by airborne measurements. *IEEE Trans. Geosci. Rem. Sens.*, 56(7),
1025 3715-3734, <https://doi.org/10.1109/TGRS.2018.2809504>, 2018.
- 1026 Shokr, M., and Markus, T.: Comparison of NASA Team2 and AES-York ice concentration algorithms against operational ice
1027 charts from the Canadian Ice Service. *IEEE Trans. Geosci. Rem. Sens.*, 44(8), 2164-2175,
1028 <https://doi.org/10.1109/TGRS.2006.872077>, 2006.
- 1029 Shokr, M., and Agnew, T. A.: Validation and potential applications of Environment Canada Ice Concentration Extractor
1030 (ECICE) algorithm to Arctic ice by combining AMSR-E and QuikSCAT observations. *Rem. Sens. Environ.*, 128, 315-332,
1031 <https://doi.org/10.1016/j.rse.2012.10.016>, 2013.
- 1032 Spreen, G., Kaleschke, L., and G. Heygster, G.: Sea ice remote sensing using AMSR-E 89-GHz channels. *J. Geophys. Res.*,
1033 113, C02S03, <https://doi.org/10.1029/2005JC003384>, 2008.
- 1034 Steer, A., Worby, A. P., and Heil, P.: Observed changes in sea-ice floe size distribution during early summer in the western
1035 Weddell Sea. *Deep-Sea Res. II*, 55, 933-942, <https://doi.org/10.1016/j.dsr2.2007.12.016>, 2008.
- 1036 Steffen, K., and Maslanik, J. A.: Comparison of Nimbus 7 scanning multichannel microwave radiometer radiance and derived
1037 sea ice concentrations with Landsat imagery for the north water area of Baffin Bay. *J. Geophys. Res.*, 93(C9), 10769-10781,
1038 <https://doi.org/10.1029/JC093iC09p10769>, 1988.
- 1039 Steffen, K. and Schweiger, A.: NASA team algorithm for sea ice concentration retrieval from Defense Meteorological Satellite
1040 Program special sensor microwave imager: comparison with Landsat satellite data. *J. Geophys. Res.*, 96(C12), 21,971-21,987,
1041 1991.
- 1042 Titchner, H. A., and Rayner, N. A.: The Met Office Hadley Centre sea ice and sea surface temperature data set, version 2: 1.
1043 Sea Ice concentrations. *J. Geophys. Res. Atmos.*, 119(6), 2864-2889, <https://doi.org/10.1002/2013JD020316>, 2014.



- 1044 Tonboe, R. T., Eastwood, S., Lavergne, T., Sørensen, A. M., Rathmann, N., Dybkjær, G., Pedersen, L. T., Høyer, J. L., and
1045 Kern, S.: The EUMETSAT sea ice concentration climate data record. *The Cryosphere*, 10(5), 2275-2290,
1046 <http://doi.org/10.5194/tc-10-2275-2016>, 2016.
- 1047 Torres, R., Snoeij, P., Geudtner, D., Bibby, D., Davidson, M., Attema, E., Potin, P., Rommen, B., Floury, N., Brown, M.,
1048 Traver, I. N., Deghaye, P., Duesmann, B., Rosich, B., Miranda, N., Bruno, C., L'Abbate, M., Croci, R., Pietropaolo, A.,
1049 Huchler, M., and Rostan, F.: GMES Sentinel-1 mission. *Rem. Sens. Environ.*, 120, 9-24,
1050 <https://doi.org/10.1016/j.rse.2011.05.028>, 2012.
- 1051 Toyota, T., Haas, C., and Tamura, T.: Size distribution and shape properties of relatively small sea-ice floes in the Antarctic
1052 marginal ice zone in late winter. *Deep-Sea Res. II*, 58, 1182-1193, <https://doi.org/10.1016/j.dsr2.2010.10.034>, 2011.
- 1053 Toyota, T., Kohout, A., and Fraser, A. D.: Formation processes of sea ice floe size distribution in the interior pack and its
1054 relationship to the marginal ice zone off East Antarctica. *Deep-Sea Res., II*, 131, 28-40,
1055 <https://doi.org/10.1016/j.dsr2.2015.10.003>, 2016.
- 1056 Tschudi, M. A., Curry, J. A., and Maslanik, J. A.: Characterization of springtime leads in the Beaufort/Chukchi Seas from
1057 airborne and satellite observations during FIRE/SHEBA. *J. Geophys. Res.*, 107(C10), 8034,
1058 <https://doi.org/10.1029/2000JC000541>, 2002.
- 1059 Wang, L., Scott, K. A., Xu, L., and Clausi, D. A.: Sea ice concentration estimation during melt from dual-pol SAR scenes
1060 using deep convolutional neural networks: A case study. *IEEE Trans. Geosci. Rem. Sens.*, 54(8), 4524-4533,
1061 <https://doi.org/10.1109/TGRS.2016.2543660>, 2016.
- 1062 Wang, L., Scott, K. A., and Clausi, D. A.: Sea ice concentration estimation during freeze-up from SAR imagery using a
1063 convolutional neural network. *Rem. Sens.*, 9(5), 408-427, <https://doi.org/10.3390/rs9050408>, 2017.
- 1064 Wang, Y.-R. and Li, X.-M.: Arctic sea ice cover data from spaceborne SAR by deep learning, *Earth Syst. Sci. Data Discuss.*
1065 [preprint], <https://doi.org/10.5194/essd-2020-332>, in review, 2020.
- 1066 Wensnahan, M., Maykut, G. A., Grenfell, T. C., and Winebrenner, D. P.: Passive microwave remote sensing of thin sea ice
1067 using principal component analysis. *J. Geophys. Res.*, 98(C7), 12453-12468, <https://doi.org/10.1029/93JC00939>, 1993.
- 1068 Wiebe, H., Heygster, G., and Markus, T.: Comparison of the ASI ice concentration algorithm with Landsat-7 ETM+ and SAR
1069 imagery. *IEEE Trans. Geosci. Rem. Sens.*, 47(9), 3008-3015, <https://doi.org/10.1109/TGRS.2009.2026367>, 2009.
- 1070 Willmes, S., Nicolaus, M., and Haas, C.: The microwave emissivity variability of snow covered first-year sea ice from late
1071 winter to early summer: a model study. *The Cryosphere*, 8(3), 891-904, <https://doi.org/10.5194/tc-8-891-2014>, 2014.
- 1072 Worby, A. P., and Comiso, J. C.: Studies of the Antarctic sea ice edge and ice extent from satellite and ship observations. *Rem.*
1073 *Sens. Environ.*, 92(1), 98-111, <https://doi.org/10.1016/j.rse.2004.05.007>, 2004.
- 1074 Zakhvatkina, N., Korosov, A., Muckenhuber, S., Sandven, S., and Babiker, M.: Operational algorithm for ice-water
1075 classification on dual-polarized RADARSAT-2 images. *The Cryosphere*, 11(1), 33-46, <https://doi.org/10.5194/tc-11-33-2017>,
1076 2017.
- 1077 Zatko, M. C., and Warren, S. G.: East Antarctic sea ice in spring: spectral albedo of snow, nilas, frost flowers and slush, and
1078 light-absorbing impurities in snow. *Ann. Glaciol.*, 56(69), 53-64, <https://doi.org/10.3189/2015AoG69A574>, 2015.
- 1079 Zhang, Q., and Skjetne, R.: Image processing for identification of sea-ice floes and the floe size distributions. *IEEE Trans.*
1080 *Geosci. Rem. Sens.*, 53(5), 2913-2924, <https://doi.org/10.1109/TGRS.2014.2366640>, 2015.
- 1081 Zhao, X., Chen, Y., Kern, S., Qu, M., Ji, Q., Fan, P., and Liu, Y.: Sea ice concentration derived from FY-3D MWRI and its
1082 accuracy assessment. *IEEE Trans. Geosci. Rem. Sens. (Early Access)*, 18 pp., <https://doi.org/10.1109/TGRS.2021.3063272>,
1083 2021.